

Highlights

Traffic-Aware Grid Planning for Dynamic Wireless Electric Vehicle Charging

Dipanjan Ghose, S Sivarajanji, Junjie Qin

- Introduces a traffic-aware grid planning framework for dynamic wireless EV charging
- Couples macroscopic traffic flow with AC-OPF for cost-efficient microgrid design
- Demonstrates the framework on real traffic data and scenarios from a US highway
- Achieves significant cost savings over worst-case planning, supporting DWC deployment

Traffic-Aware Grid Planning for Dynamic Wireless Electric Vehicle Charging

Dipanjan Ghose^{a,*}, S Sivaranjani^b, Junjie Qin^a

^a*Elmore Family School of Electrical and Computer Engineering, Purdue University, West Lafayette, Indiana, USA*
^b*Edwardson School of Industrial Engineering, Purdue University, West Lafayette, Indiana, USA*

Abstract

Dynamic Wireless Electric Vehicle Charging (DWC) on electrified roadways is an emerging technology that can significantly reduce battery sizes, eliminate charging downtime, and alleviate range anxiety, specially for long-haul transportation and fleet operations of electric vehicles (EVs). However, these systems introduce new challenges for power system planning due to their short-duration and high-power demands which can strain the grid if not properly managed. As the energy demands from DWC depend on vehicle speed, density, dwell time in charging zones, and load profiles along road segments, there is a need for integrated planning of such systems, jointly considering both traffic behavior and EV energy consumption. In this paper, we propose a traffic-aware grid planning framework for DWC. We leverage a macroscopic Cell Transmission Model of traffic flow to estimate real-time, spatiotemporal EV charging demand from DWC corridors. The demand model is then integrated into an AC Optimal Power Flow based formulation to optimally size a microgrid that supports DWC under varying traffic conditions while minimizing the cost of operation. Our framework explicitly models how spatiotemporal traffic patterns affect the utilization of grid resources to obtain system designs that achieve lower costs and are easier to operationalize as compared to planning models that rely on worst-case traffic data. We demonstrate the framework on data from a 14-mile segment of the I-210W highway in California, USA, evaluating multiple traffic scenarios like free-flow, severe congestion, accidents of varying severity, and natural disasters like forest fires. Our results demonstrate that traffic-aware grid planning significantly reduces infrastructure costs as compared to worst-scenario based modeling, while ensuring reliability of service in terms of meeting charging demands under diverse traffic conditions.

Keywords: Electric Vehicles, Dynamic Wireless Charging, Traffic Flow, Dynamic Electric Vehicle Charging, Microgrid Planning, Power Flow

1. Introduction

Vehicle electrification has become a key pillar in global efforts towards achieving sustainable transportation infrastructures. However, widespread electric vehicle (EV) adoption still faces significant barriers, including limited access to charging infrastructure, high upfront vehicle costs, and

*Corresponding author

Email addresses: dghose@purdue.edu (Dipanjan Ghose), sseetha@purdue.edu (S Sivaranjani), jq@purdue.edu (Junjie Qin)

consumer concerns such as range anxiety. Dynamic Wireless Electric Vehicle Charging (DWC) on electrified roadways offers a promising solution to several of these challenges. By enabling vehicles to charge while in motion, DWC reduces charging downtime by minimizing the need for frequent plug-in stops. Multiple vehicles can charge simultaneously along the same roadway segment, reducing congestion at stationary charging stations [1]. Since DWC systems utilize existing road infrastructure, they avoid the need for additional land use or extensive construction. Moreover, they provide utilities with greater flexibility and control over charging demand, thereby improving grid reliability [2]. By ensuring consistent access to charging during travel, DWC also reduces size requirements for onboard batteries, potentially lowering both the cost and weight of future EVs.

Owing to these potential advantages, DWC is receiving increasing attention around the world, with multiple pilot projects underway [3, 4, 5, 6]. Despite successful pilot deployments, DWC still faces a distinct and underexplored set of barriers compared to conventional EV charging. In contrast to static charging, DWC must deliver high-power, uninterrupted energy transfer to vehicles in motion, where both the supply and demand conditions change continuously. This makes DWC not just a more complex technical challenge, but a fundamentally different problem that current charging and grid-integration models are not well-suited to address. Specifically, DWC demand profiles are dictated by real-time traffic flow patterns, creating spatiotemporal fluctuations driven by factors such as vehicle density, instantaneous power requirements of individual EVs, lane-level positioning, and even less quantifiable human behaviors like braking patterns, lane changing, and inter-vehicular spacing. The result is that DWC demand is volatile, highly non-uniform, and difficult to predict. Thus, DWC cannot be treated as a simple extension of static charging. Instead, it represents a new paradigm where transportation networks and power systems are tightly coupled, necessitating a framework that explicitly incorporates traffic flow variability into power system design to ensure reliability of service and optimal utilization of the grid infrastructure.

Coupling transportation networks and power grids for DWC naturally raises several important questions. *How can we accurately model the energy demand imposed by traffic flow, given the inherent variability and unpredictability of vehicle movements? How do these demand patterns influence the design and operation of the supporting power grid? How do we guarantee reliable service under varying traffic conditions?* A seemingly intuitive approach would be to monitor the power requirements of every vehicle on the road and simply aggregate them to obtain total demand, ensuring that the grid can always meet the cumulative load. However, in practice, such microscopic (agent-level) modeling is computationally expensive, impractical at scale, and raises non-trivial concerns around consumer privacy. These challenges motivate our proposed approach: a novel planning framework that leverages macroscopic traffic models rather than vehicle-level monitoring, and integrates these models directly with grid planning to design DWC infrastructures that are both efficient and reliable.

The reasoning behind utilizing macroscopic traffic flow models for grid planning is as follows. Vehicle movements on the road arise from the interplay of multiple complex factors, including road geometry, individual vehicle characteristics, and driver behavior. While each vehicle follows its own unique power demand profile based on these factors, many traffic parameters, such as speed and vehicle density, tend to average out across space and time at larger scales [7]. Drawing on analogies with fluid dynamics, macroscopic traffic flow models capture overall system behavior using a compact set of equations, offering both scalability for large networks and tractability for simulation. They also reduce the reliance on individual vehicle data, mitigating both computational and privacy concerns. The underlying assumption is that in a system designed to satisfy prescribed reliability requirements, small fluctuations in individual vehicle behavior will have limited influence

on aggregate system performance.

In this work, we develop a *traffic-aware grid planning framework* that couples macroscopic traffic flow patterns with power grid models to design infrastructure that can reliably support DWC. We utilize the Cell Transmission Model (CTM) of traffic flow [8] to estimate average traffic densities in different roadway segments, which then forms the basis for predicting roadway-level energy demand. By explicitly incorporating spatiotemporal variations in traffic behavior, we investigate how DWC-enabled roadways can be integrated into grid operations, not only to meet charging demand but also to provide flexibility in generation planning and potentially participation in ancillary grid services in the future. Our approach embeds realistic, traffic-driven macroscopic loads into microgrid design, enabling infrastructure that is operationally robust and reliable under real-world traffic conditions.

1.1. Literature Survey

Conceptually, wireless charging of EVs has been explored for several decades, but its potential as a commercially viable charging technology emerged more recently (see [9, 10] for a comprehensive survey). Despite its early inception, the adoption of DWC systems has remained limited, with most projects worldwide restricted to small-scale pilots and experimental demonstrations under controlled conditions. A major barrier to broader deployment is the absence of a consistent framework that links the planning and design of DWC infrastructure with the real-time charging demands arising from traffic flow [1]. Owing to their dynamic and unpredictable nature, DWC loads introduce unique complexities in infrastructure planning and grid integration. While aggregate load curves resemble those of static charging at a coarse scale, their overall operation is fundamentally different. Sauter et al. note that DWC's transient loads contrast sharply with the more predictable patterns of static charging [11]. Static EV charging and its grid impacts have been extensively studied [12, 13], whereas comparable studies on DWC remain at an early stage.

One line of approaches for DWC control is the microscopic regulation of individual vehicle characteristics. For instance, some methods initiate charging based on a minimum state-of-charge (SoC) threshold [14], while others assume uniform energy consumption across vehicles according to distance traveled [15]. Wang et al. propose a strategy that assigns priority values to EVs based on their battery levels, incorporating different car-following models [16]. Similarly, Majidi and Parvania suggest a strategy in which DWC controllers use route and traffic information to estimate vehicle power requests [17]. However, these approaches remain centered on individual vehicle behavior and assume detailed information, such as SoC and speed of every vehicle is always available, which is often impractical in real-world settings due to data accessibility constraints.

Similar efforts have optimized charging power allocation by scheduling DWC buses [18], but these approaches often neglect the stochastic nature of traffic and instead rely on fixed speed profiles [19]. More broadly, most works that incorporate traffic flow either emphasize microscopic vehicle behavior or restrict analysis to small-scale, homogeneous networks within confined geographic areas [20]. Experimental studies have also proposed strategies such as dedicated charging lanes for slow-moving traffic [21] or incentive-based schemes that reward EVs for following traffic guidelines to regulate charging demand [22]. However, such approaches are difficult to scale along long-distance corridors and typically overlook the impact of charging demand on the underlying power grid and its operational constraints.

Karakitsios et al. incorporated grid constraints by proposing a simple on-off control strategy for wireless chargers, activating segments only when surplus power was available [23]. While this respects grid operational limits, it restricts DWC's reliability as a charging solution due to its dependence on excess capacity. More generally, many joint planning efforts overlook critical system

constraints. For instance, Sun et. al. [24] optimize DWC infrastructure placement without accounting for generation or transmission limits, whereas Aduama et. al. [25] design grids for bus fleets which follow highly predictable and scheduled routes which does not capture the varying traffic behavior in general-purpose DWC. Majidi and Parvania partially address this gap by incorporating EV routes and traffic densities into a grid simulation framework [26]; however, they do not address the problem of grid planning to support DWC.

Thus, the intersection of traffic flow modeling and operational planning of the associated grid infrastructure remains an area with significant gaps, forming the focus of our work. We model demand using well-defined macroscopic traffic flow dynamical models that capture the variations in real-time traffic while remaining independent of the fluctuations in individual vehicle behavior. Building on this model, we address the problem of planning a supporting microgrid infrastructure by formulating and solving optimization problems for both energy storage (ES) and solar generation siting and sizing, while rigorously accounting for voltage limits, power flows, and capacity constraints as encoded by an AC Optimal Power Flow (AC-OPF) model [27]. We solve the planning problem for variety of realistic traffic scenarios, ranging from normal traffic to extreme events, to obtain a resilient grid design capable of meeting charging demand under varying conditions.

1.2. Major Contributions

The main contributions of this work can be summarized as follows:

1. We develop a traffic-aware dynamic energy consumption modeling framework that captures the physics of macroscopic traffic flow to estimate the spatiotemporal energy demand of EVs across roadway segments. Our proposed model is independent of microscopic vehicle characteristics and individual driving behavior. Rather, we leverage macroscopic traffic flow theory, which enhances scalability and avoids the need for detailed vehicle-level data.
2. We leverage this traffic-aware energy consumption model towards operational planning of a microgrid to support DWC. Specifically, we couple the macroscopic traffic model with a Second-Order Cone Programming (SOCP) relaxation of the AC-OPF problem to optimize the design and operation of a microgrid to support DWC. To enhance system resilience, we model traffic flow under several realistic roadway scenarios including day-to-day variations, accidents, lane closures, and extreme events like wildfires.
3. As part of the microgrid planning framework, we also solve an ES placement problem which includes optimizing the number and location of ES units based on their unit capacities, charge/discharge power limits, contributions to locational voltage support, and their role in maintaining grid stability over the defined operational period.
4. We demonstrate through realistic case studies on data from the I210-W in California that incorporating information on traffic-aware models of DWC demand enables more efficient grid planning by avoiding unnecessary oversizing and reducing capital and infrastructure investments to support DWC. This is validated by comparing the resulting infrastructure costs for grid planning with and without traffic-aware energy demand modeling.

To the best of our knowledge, this work is among the first to integrate macroscopic traffic flow theory with OPF and microgrid planning to design robust and resilient DWC grid infrastructure. Unlike previous approaches that rely on either microscopic vehicle-level modeling or static assumptions about charging demand, our framework captures the aggregate behavior of traffic and

translates it directly into grid-level planning decisions. This framework also provides a practical tool for grid planners and policymakers to estimate the size, capacity, and operational flexibility of DWC systems under realistic traffic conditions. Furthermore, by embedding traffic-driven loads into grid planning, this paradigm can eventually support the integration of DWC with other energy services, including demand response programs and participation in ancillary electricity markets, offering a pathway toward more resilient and efficient energy systems.

1.3. Organization of the Paper

The remainder of the paper is organized as follows. Section 2 presents a motivating example illustrating the need for traffic-aware DWC demand modeling. Section 3 introduces our problem formulation and the key assumptions used throughout the study. Section 4 details the traffic flow models that form the basis of our demand estimation. Section 5 presents the proposed grid planning and optimization problem taking into account the traffic-aware demand models from Section 4. In Section 6, we describe the case study using data from the I-210 W highway in the Greater Los Angeles area of California, which is followed in Section 7 by detailed results from the traffic simulations and validation studies. Finally, Section 8 discusses the findings and concludes the paper.

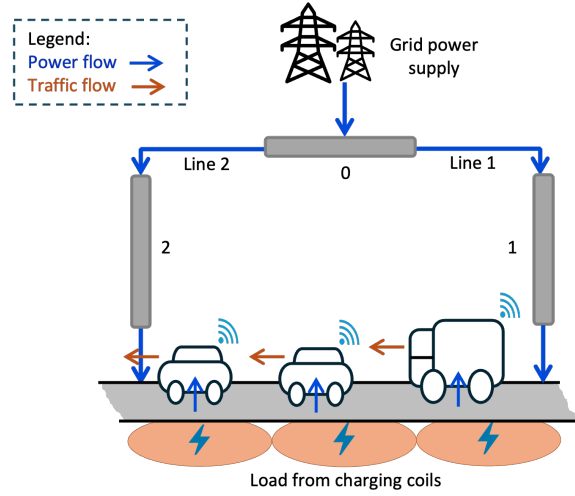
2. Motivating Example

Consider a simple three-bus system as shown in Fig. 1(a) where the load corresponds to the DWC demand arising from a roadway segment. Charging pads are embedded beneath a designated charging lane, with power transmitters connected to the two buses located at either end of this segment (Buses 1 and 2), which are in turn connected to a central Bus 0 that interfaces directly with the main power grid. The objective here is to demonstrate that incorporating traffic flow dynamics into the modeling framework can influence system costs, even in the most basic setting. While the remainder of the paper addresses a planning problem that leverages the flexibility inherent in traffic patterns, this simple example assumes that roadway demand is supplied directly by the grid with unlimited capacity. Under this assumption, we evaluate the cost implications using a quadratic cost function, which is standard in most electricity market formulations. The cost of procuring electricity to serve the demand on this DWC segment is defined as:

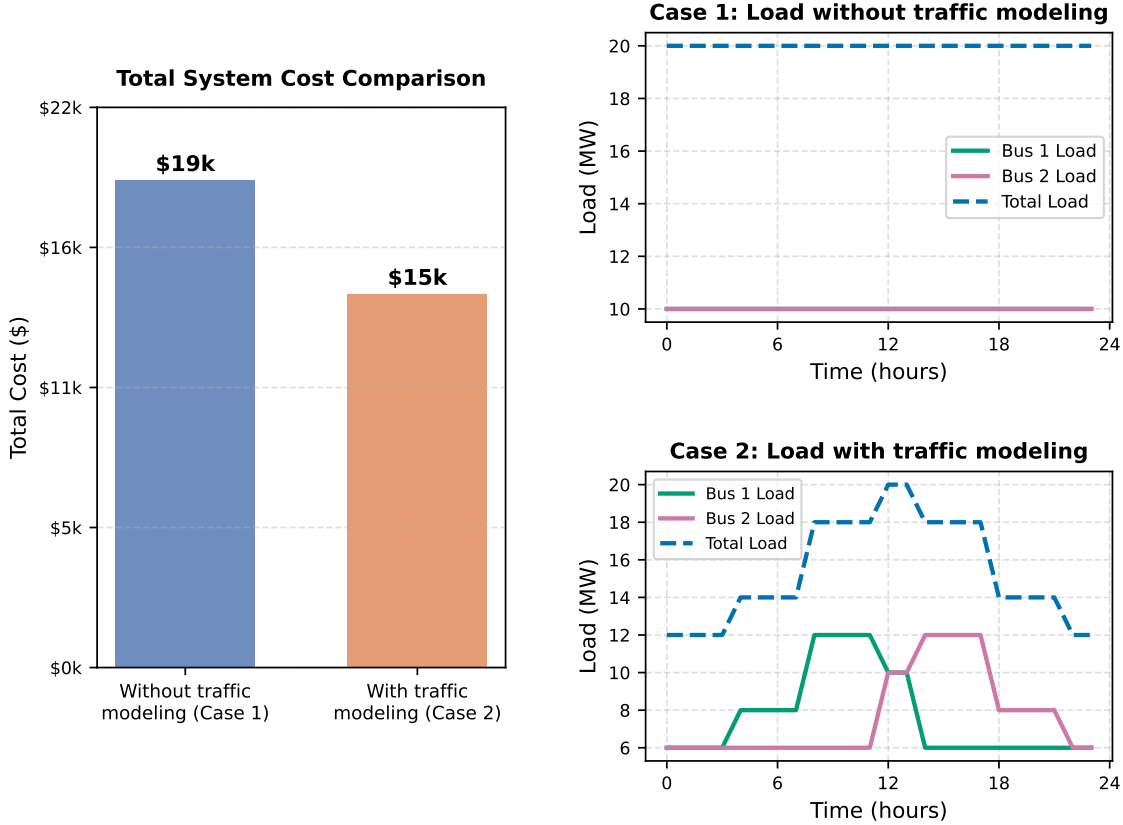
$$C_{\text{electricity}} = \sum_{t \in \mathcal{T}} a \cdot E_{\text{demand}}^{(t)} + b \cdot \left(E_{\text{demand}}^{(t)} \right)^2, \quad (1)$$

where $E_{\text{demand}}^{(t)}$ denotes the total energy demand (MWh) from the DWC coils at time step t , with the time step size being chosen as 1 hour. The total cost $C_{\text{electricity}}$ is obtained by summing the costs across all time steps within the operating horizon \mathcal{T} , which is set to be 24 hours in this example, with a and b denoting the cost coefficients, fixed at \$40/MWh and \$0.002/MWh, respectively. To evaluate the impact of traffic-aware modeling, we compare two cases, as illustrated in Figure 1(b) and defined below:

- **Case 1:** The charging demand is represented as a constant load, corresponding to the worst-case scenario of maximum expected traffic demand. This reflects a common practice in existing planning approaches, where demand is assumed to remain fixed over time, independent of real-time traffic variations. The total load is set to 20 MW, uniformly distributed between Bus 1 and Bus 2.



(a) Illustrative three-bus example system for testing the traffic-driven demand theory for DWC planning.



(b) Results demonstrating the impact of considering the dynamics of traffic flow on system demand (as shown by the two demand plots Case 1 and case 2) and overall cost (as shown by the total system cost comparison plot).

Figure 1: Example system illustrating the influence of traffic flow dynamics on roadway energy demand.

- **Case 2:** The charging demand is modeled as a distributed, time-varying load that more closely reflects real-time traffic conditions. In this case, the cumulative 20 MW peak is reached only for a brief period during the day. On typical workdays, traffic peaks occur at different locations along the roadway as people commute to and from work. Following this pattern, we model the traffic peak alternatively at Buses 1 and 2 in the morning and again in the evening. Midday corresponds to the cumulative peak, where the total load reaches 20 MW, matching the worst-case scenario of Case 1. The load profile for this scenario is illustrated in Fig. 1(b). In other words, the day begins with low traffic flow during late-night and early-morning hours, followed by morning and afternoon peaks, resulting in the cumulative midday peak that aligns with the maximum demand set earlier.

Then, the objective is to determine the amount of power drawn from the external grid under both scenarios. Using the electricity cost function defined in (1) and the load profiles from the two cases, the total system cost comparison in Fig. 1(b) reveals a significant reduction in electricity costs of nearly 23.3% for Case 2, where traffic-aware modeling was applied. In contrast, Case 1 assumes continuous worst-case demand, which leads to persistent over-provisioning resulting in unnecessary costs. This setup mirrors a conventional planning approach in which the system is sized to meet continuous worst-case demand, rather than being designed based on realistic traffic flows, where the peak is only reached briefly during the day.

This example illustrates the significant oversizing and associated cost penalties that arise when relying on constant, worst-case demand estimates. Even with a basic, intuitive traffic profile, integrating realistic traffic dynamics significantly decreases electricity costs. In a scaled-up system, with longer operating horizons and multiple roadway segments, this difference in costs between constant demands and traffic-aware demands will amount to millions of dollars, making it critical to consider spatio-temporal variations in traffic demands for DWC grid planning. Moreover, incorporating traffic models into grid planning provides the potential to coordinate flexible resources such as solar generation and ES with traffic patterns (e.g., charging the ES during low-demand periods and discharging during peak traffic loads) to obtain significant savings in both capital and operational expenditures. This example motivates the developments in the remainder of this paper, where we examine the traffic–energy coupling in greater detail and show how it can improve both planning and operation of DWC power infrastructure.

3. Model Overview and Assumptions

Traffic-aware grid planning involves two main components. The first is the modeling of macroscopic traffic flow, for which we leverage the Cell Transmission Model (CTM). The CTM describes the dynamics of traffic density evolution across discrete segments of the roadway, from which both the number of EVs and the average traffic velocity at each location and time step can be inferred. This information is then used as input to a dynamic EV energy consumption model, which estimates per-vehicle energy demand based on average values for key physical parameters such as powertrain efficiency, vehicle mass, frontal area, drag coefficient, and rolling resistance. By combining the CTM output with the energy consumption model, we can compute the total energy demand imposed on each roadway segment over time, providing a traffic-aware load profiles for grid planning and operational analysis.

These spatio-temporal load profiles are then used for planning of a microgrid to support DWC. The microgrid is assumed to consist of distributed energy resources including solar generation, ES

units, and a coupling with the external grid. The grid planning problem accounts for both capital and operational costs over the lifetime of the infrastructure as well as key grid constraints including voltage limits, power balance, and thermal capacity on lines. We note that we do not account for factors like growth in EV penetration and expansions in highway infrastructure for this study, as the focus is on the immediate impact of traffic flow on energy demand and microgrid planning. A flowchart representing the overall methodology is shown in Fig. 2. To evaluate the proposed framework, we consider a case study involving multiple traffic scenarios where each scenario represents a unique spatiotemporal energy demand profile (e.g., lane closure, accident) along the highway, which is then used to assess the corresponding operational reliability of the microgrid.

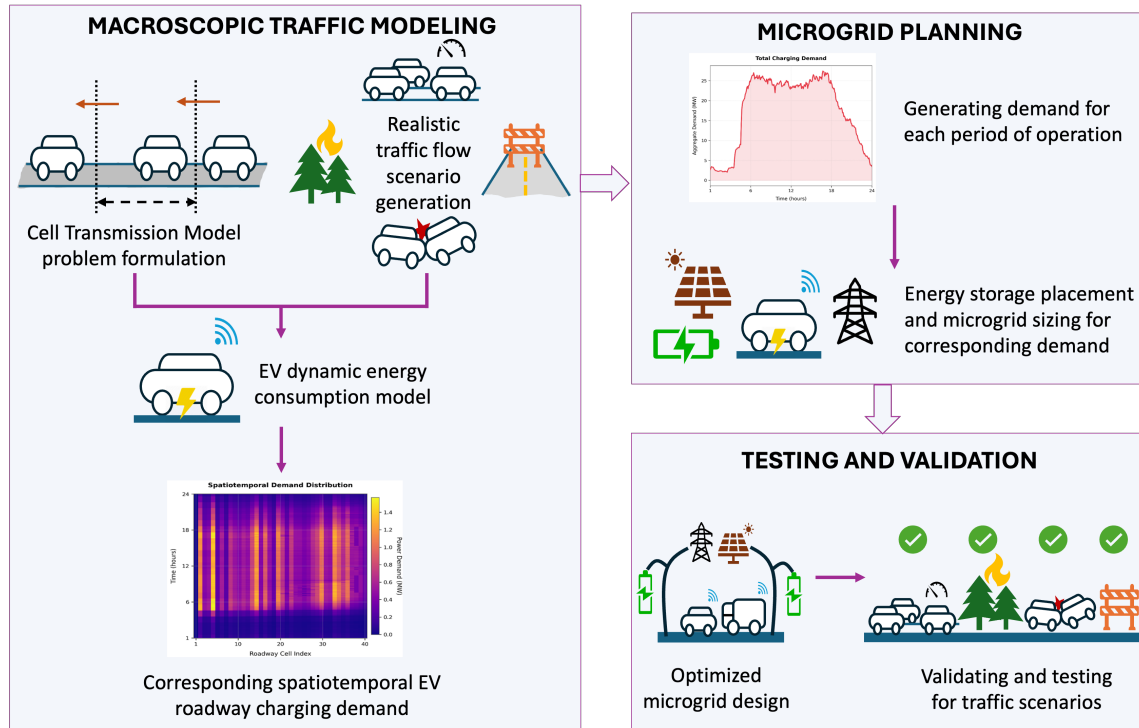


Figure 2: Proposed methodological framework for traffic-aware grid planning in the DWC system.

4. Traffic-Aware Energy Demand Modeling

4.1. Cell Transmission Model

The dynamics of large-scale macroscopic traffic flow have been extensively studied over the past few decades, leading to the development of several models for traffic analysis. Among these, the CTM, introduced by Daganzo in 1994 [8], stands out as one of the most widely adopted frameworks for modeling multi-commodity traffic flow across complex networks [28]. We adopt the CTM for our setting as its discrete, computationally efficient formulation and its ability to capture key traffic phenomena such as congestion, shockwaves, and spillback [29] make it particularly well-suited for large-scale planning. Unlike microscopic agent-level models of EV traffic, the CTM avoids the need

for detailed vehicle-level data, making it more scalable and practical for integration with energy system planning.

In the CTM, the road network is segmented into a series of cells, and time is divided into discrete intervals. The length of each cell is defined as the distance a vehicle would travel in a single timestep under free-flow (no congestion) conditions, ensuring that all vehicles within a cell advance to the next cell at every timestep [8, 30]. Individual vehicle characteristics, such as velocity, are assumed to average out over the spatial and temporal scales of a cell and are effectively treated as constants within each cell.

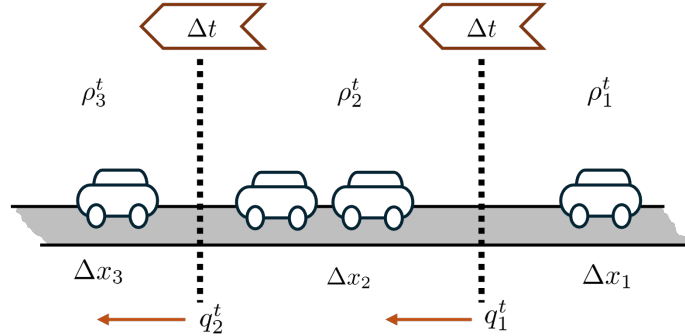


Figure 3: Key roadway traffic components represented in the CTM-based traffic flow formulation.

Consider a representative roadway network for the CTM formulation as shown in Fig. 3. The update equation for vehicle density (vehicles per mile of road) in a cell at each time step is derived from a mass conservation law for the number of vehicles and the fundamental principles of macroscopic traffic flow theory. The density of vehicles in each cell i at time step t , denoted by $\rho_i^{(t)}$ evolves as [8]:

$$\rho_i^{(t+1)} = \rho_i^{(t)} + \frac{\Delta t}{\Delta x_i} (q_{i-1}^{(t)} - q_i^{(t)}), \quad (2)$$

where $q_i^{(t)}$ denotes the traffic flow (in vehicles per hour) in cell i , and Δt and Δx_i denote the time step size and the length of cell i respectively. The change in density within each cell is governed by the difference between the incoming and outgoing flows, where the flow $q_i^{(t)}$ is written as

$$q_i^{(t)} = \min(d_i^{(t)}, s_{i-1}^{(t)}), \quad (3)$$

where $d_i^{(t)}$ and $s_i^{(t)}$ represent the demand (receiving capacity) and supply (sending capacity) of the cells at a given timestep, respectively, given by:

$$d_i^{(t)} = \begin{cases} Q(\rho_i) & \text{if } \rho_i \leq \rho_{\text{crit},i}, \\ q_{\text{cap},i} & \text{if } \rho_i > \rho_{\text{crit},i}, \end{cases} \quad (4)$$

$$s_i^{(t)} = \begin{cases} Q(\rho_i) & \text{if } \rho_i > \rho_{\text{crit},i}, \\ q_{\text{cap},i} & \text{if } \rho_i \leq \rho_{\text{crit},i}. \end{cases} \quad (5)$$

Here, $Q(\rho_i)$ represents a piecewise affine approximation of the relationship between traffic flow and density in the fundamental diagram of traffic ([8, 30]), given by

$$Q(\rho_i) = \begin{cases} v_{\text{ff},i} \cdot \rho_i & \text{if } \rho_i \leq \rho_{\text{crit},i}, \\ w_i \cdot (\rho_{\text{jam},i} - \rho_i) & \text{if } \rho_i > \rho_{\text{crit},i}, \end{cases} \quad (6)$$

with

$$q_{\text{cap},i} = \rho_{\text{crit},i} \times v_{\text{ff},i}, \quad (7)$$

and $v_{\text{ff},i}$ and w_i representing the free-flow speed (maximum speed in uncongested conditions) and the congested wave speed (rate at which congestion propagates upstream) respectively, $\rho_{\text{jam},i}$ denoting the jamming density at which traffic is in standstill, and $\rho_{\text{crit},i}$ denoting the critical density at which traffic flow reaches its peak capacity. These parameters are calibrated for each cell based on historical data of traffic behavior and vehicle characteristics in that roadway section. The inflows and outflows to each cell can also be augmented with traffic flows entering through on-ramps and exiting through off-ramps (see [30] for details). The CTM integrates (2)-(7) to determine vehicle density at each cell for every timestep.

4.2. Dynamic Energy Consumption Model

We now develop a dynamic energy consumption model that captures the coupling between traffic flow dynamics and the corresponding energy demand, forming the basis for microgrid planning. Our main contribution in this section lies in translating vehicle density and speed data from the CTM into the corresponding average estimated loads for the power grid. It is important to note that while energy demand may intuitively appear to scale proportionally with vehicle density, this is not the case. Observing the dynamics of traffic flow in the CTM from (2)-(7), we see that the density of vehicles in each cell is nonlinearly related to the traffic flows through congestion-dependent demand profiles as in (4), where vehicle speed drops sharply once traffic density exceeds a critical threshold. Therefore, in order to accurately estimate the demand on the grid, we should consider the underlying dynamics of the traffic density, which evolves as a nonlinear function of traffic speed and congestion.

The first element in this formulation is the driving energy required for individual vehicles. The power needed to drive a certain distance depends on several vehicular parameters, such as mass, frontal area, speed, and efficiency, as well as physical factors like air resistance and rolling resistance of the wheels. In general, the driving power $p_{\text{drive},i}$ for individual vehicles i at timestep t is calculated using the following relation [31]:

$$p_{\text{drive},i}^{(t)} = \frac{1}{\eta_{\text{drive}}} \cdot \left(\frac{1}{2} C_d A \rho_{\text{air}} (v_i^{(t)})^3 + C_{\text{rr}} m g v_i^{(t)} \right), \quad (8)$$

where $p_{\text{drive},i}$ is the average instantaneous power required by a HEV to drive, $v_i^{(t)}$ is the average velocity obtained for the cell at timestep t from the CTM, η_{drive} is the efficiency of the electric drivetrain, C_d is the drag coefficient, C_{rr} is the rolling resistance coefficient, A is the average frontal area of an HEV, ρ_{air} is the air density, m is the average mass of the EV, and g is the acceleration due to gravity.

To determine the actual power required from the DWC coils, we also account for auxiliary power consumption, denoted by p_{aux} which includes factors such as air conditioning. Then, the

total energy consumption for a single vehicle in cell i at timestep j is given by:

$$e_{\text{drive},i}^{(t)} = (p_{\text{drive},i}^{(t)} + p_{\text{aux}}) \cdot \Delta t, \quad (9)$$

where $p_{\text{drive},i}^{(t)}$ is the driving power calculated according to (8). To scale this up to macroscopic traffic flow, we multiply the single-vehicle energy consumption by the time-varying number of vehicles in each cell at timestep t , yielding:

$$E_{\text{drive},i}^{(t)} = e_{\text{drive},i}^{(t)} \cdot \rho_i^{(t)} \cdot \Delta x_i, \quad (10)$$

where $\rho_i^{(t)}$ evolves according to the CTM in (2)-(7), capturing spatio-temporal demand under varying traffic conditions. Finally, we include the additional energy required for charging on-board batteries in the EV, resulting in the total energy consumption of the DWC charging coils given by:

$$E_{\text{coil},i}^{(t)} = E_{\text{drive},i}^{(t)} + (SoC_{\text{mile}} \cdot \Delta x_i \cdot E_{\text{battery}} \cdot (\rho_i^{(t)} \Delta x_i)), \quad (11)$$

where SoC_{mile} is the per-mile energy demand to increase the SoC of the on-board EV battery, and E_{battery} is the average battery capacity of the EV. Note that SoC_{mile} can also be dynamically adjusted based on resource availability at any given timestep, enabling flexibility in energy allocation and system responsiveness to real-time conditions.

This formulation provides a traffic-aware model for calculating the total energy demand generated at each cell of the roadway at every timestep, accumulating the driving, auxiliary, and charging energy of the vehicles. Notice that the energy consumption in (11) depends on the dynamics of vehicle density in each cell which in turn depends nonlinearly on the traffic speeds and congestion as described in the CTM, thus capturing spatio-temporal variations in grid demand across varying traffic conditions.

5. System Design and Optimization

In the previous section, we developed a dynamic energy consumption model defines roadway demand. In this section, we will leverage this energy consumption model for microgrid planning.

5.1. System Sizing

The planning problem for DWC grid infrastructure can be viewed as a bi-level optimization with inner and outer level problems. The inner problem focuses on the day-to-day operation of the microgrid, ensuring that it meets the fluctuating demand from the dynamic charging coils while satisfying all grid constraints. The outer level problem handles long-term planning by optimizing the capital investment in key components, namely the solar and ES units, and the coupling with the main power grid. The solution of the inner operational problem across a defined time horizon feeds into the outer planning problem across a given planning period, allowing us to determine the most cost-effective and reliable design for the microgrid.

Inner Operational Problem: We first formulate the daily operational problem based on an SOCP relaxation of the AC-OPF formulation [27]. This formulation is particularly well-suited for radial distribution networks and provides a convex approximation to the original non-convex AC-OPF problem. The key variables in the formulation include the squared voltage magnitude at each bus v_i , the complex power flow $S_{ij} = P_{ij} + jQ_{ij}$ from bus i to j , and the squared current magnitude l_{ij}

on line (i, j) . Each line has an impedance $z_{ij} = r_{ij} + jx_{ij}$, where r_{ij} and x_{ij} denote resistance and reactance, respectively. The load comprises the EV charging demand, while solar generation, ES dispatch, and external grid import form the generation side. The operational optimization problem is defined as follows:

$$\mathcal{J}_{\text{operational}} = \min \sum_{t \in \mathcal{T}_n} \left[\sum_{g \in \mathcal{G}} \left(a_g \cdot \left(P_g^{(t)} \right)^2 + b_g \cdot P_g^{(t)} + c_g \right) + \lambda_{\text{cycling}} \sum_{i \in \mathcal{B}} \left(P_{\text{ch},i}^{(t)} + P_{\text{dis},i}^{(t)} \right) \right], \quad (12a)$$

subject to: *Power Balance Constraints:*

$$\sum_{g \in \mathcal{G}_i} P_g^{(t)} + P_{\text{dis},i}^{(t)} + \gamma^{(t)} P_{\text{solar},i} - \left(P_{\text{load},i}^{(t)} + P_{\text{ch},i}^{(t)} \right) = \sum_{(i,j) \in \mathcal{E}} P_{i,j}^{(t)} + \sum_{(i,j) \in \mathcal{E}} r_{ji} \cdot l_{ij}^{(t)}, \quad \forall i \in \mathcal{N}, \forall t \in \mathcal{T}_n \quad (12b)$$

$$\sum_{g \in \mathcal{G}_i} Q_g^{(t)} + Q_{\text{ES},i}^{(t)} + Q_{\text{solar},i}^{(t)} - Q_{\text{load},i}^{(t)} = \sum_{(i,j) \in \mathcal{E}} Q_{i,j}^{(t)} + \sum_{(i,j) \in \mathcal{E}} x_{ij} \cdot l_{ij}^{(t)}, \quad \forall i \in \mathcal{N}, \forall t \in \mathcal{T}_n \quad (12c)$$

Voltage Constraints:

$$v_j^{(t)} = v_i^{(t)} - 2 \left(r_{ij} P_{ij}^{(t)} + x_{ij} Q_{ij}^{(t)} \right) + (r_{ij}^2 + x_{ij}^2) \cdot l_{ij}^{(t)}, \quad \forall (i, j) \in \mathcal{E}, \forall t \in \mathcal{T}_n \quad (12d)$$

$$\left\| \begin{array}{c} 2P_{ij}^{(t)} \\ 2Q_{ij}^{(t)} \\ l_{ij}^{(t)} - v_i^{(t)} \end{array} \right\|_2 \leq l_{ij}^{(t)} + v_i^{(t)}, \quad \forall (i, j) \in \mathcal{E}, \forall t \in \mathcal{T}_n \quad (12e)$$

$$v_i^{\min} \leq v_i^{(t)} \leq v_i^{\max}, \quad \forall i \in \mathcal{N}, \forall t \in \mathcal{T}_n \quad (12f)$$

Line Flow Constraints:

$$l_{ij}^{(t)} \leq \bar{l}_{ij}, \quad \forall (i, j) \in \mathcal{E}, \forall t \in \mathcal{T}_n \quad (12g)$$

Power Bounds:

$$\begin{aligned} 0 \leq P_g^{(t)} &\leq \bar{P}_g, & -\bar{Q}_g \leq Q_g^{(t)} \leq \bar{Q}_g, & \forall g \in \mathcal{G}_i, \forall t \in \mathcal{T}_n \\ 0 \leq P_{\text{solar},i} &\leq \bar{Q}_{\text{solar},i} \leq Q_{\text{solar},i}^{(t)} \leq \bar{Q}_{\text{solar},i}, & & \forall i \in \mathcal{S}, \forall t \in \mathcal{T}_n \end{aligned} \quad (12h)$$

ES Power Constraints:

$$0 \leq P_{\text{ch},i}^{(t)} \leq \bar{P}_{\text{ch},i} \cdot N_i^{\text{ES}}, \quad 0 \leq P_{\text{dis},i}^{(t)} \leq \bar{P}_{\text{dis},i} \cdot N_i^{\text{ES}}, \quad \forall i \in \mathcal{B}, \forall t \in \mathcal{T}_n, \forall N_i^{\text{ES}} \in \mathbb{Z}_{\geq 0} \quad (12i)$$

Energy Dynamics and Storage Limits:

$$E_i^{(t)} = E_i^{(t-1)} + \Delta t \cdot \left(\eta_{\text{ch}} \cdot P_{\text{ch},i}^{(t)} - \frac{1}{\eta_{\text{dis}}} \cdot P_{\text{dis},i}^{(t)} \right), \quad \forall i \in \mathcal{B}, \forall t \in \mathcal{T}_{n-1}, \quad (12j)$$

$$E_i^{(0)} = E_i^{(n)}, \quad (12k)$$

$$\begin{aligned} 0 \leq E_i^{(t)} &\leq \bar{E}^{\text{unit}} \cdot N_i^{\text{ES}}, \\ -Q_{\text{ES}}^{\text{lim}} \cdot N_i^{\text{ES}} &\leq Q_{\text{ES},i}^{(t)} \leq Q_{\text{ES}}^{\text{lim}} \cdot N_i^{\text{ES}}, \quad \forall i \in \mathcal{B}, \forall t \in \mathcal{T}_n, \forall N_i^{\text{ES}} \in \mathbb{Z}_{\geq 0} \end{aligned} \quad (12l)$$

The primary objective of this problem is to minimize total generation cost denoted by $\mathcal{J}_{\text{operational}}$. Since both solar generation and ES are renewable resources with negligible marginal operating costs, their costs are assumed to be zero. Accordingly, the objective function is defined as given by equation (12a) where a_g, b_g, c_g denote the external grid-specific cost coefficients. The second term in (12a) introduces a soft penalty on battery cycling to discourage simultaneous charging and discharging operations. We now examine the constraints, the first of which are the active and reactive power balance constraints given by equations (12b) and (12c). These constraints maintain nodal power balance across all buses $i \in \mathcal{N}$ at each time step $t \in \mathcal{T}_n$, where $\mathcal{T}_n = \{0, 1, \dots, n\}$ and n is the total number of timesteps. The equations account for the net generation, storage activity, solar output, line flows, and ohmic losses. Here, $P_g^{(t)}$ and $Q_g^{(t)}$ denote the real and reactive power generation from generator $g \in \mathcal{G}_i$, where \mathcal{G}_i is the set of generators connected to bus i . The terms $P_{\text{dis},i}^{(t)}$ and $P_{\text{ch},i}^{(t)}$ represent the discharge and charge power from the ES unit at bus i , while $Q_{\text{ES},i}^{(t)}$ is its reactive power contribution. The variable $P_{\text{solar},i}$ is the installed solar capacity at bus i , and $\gamma^{(t)} \in [0, 1]$ is the normalized solar availability factor at time t . The term $Q_{\text{solar},i}^{(t)}$ denotes the reactive power generated by the solar inverter. Real and reactive power demands at each bus are represented by $P_{\text{load},i}^{(t)}$ and $Q_{\text{load},i}^{(t)}$. The set \mathcal{E} refers to the network's total set of lines.

For each time step $t \in \mathcal{T}_n$, the voltage drop across each line $(i, j) \in \mathcal{E}$ is modeled using the branch flow formulation in (12d). Note that the original relationship between the branch current and power in the AC OPF is non-convex, given by

$$l_{ij}^{(t)} = \frac{\left(P_{ij}^{(t)}\right)^2 + \left(Q_{ij}^{(t)}\right)^2}{v_i^{(t)}}. \quad (13)$$

To ensure tractability, we adopt a SOCP relaxation of (13) as introduced in [27] to obtain constraint equation (12e). Thus, our formulation retains the exact voltage drop equation as in (12d) alongside the relaxed constraint in (12e).

For safe system operation, we also impose the set of operating constraints in equations (12f)–(12h). Here, \mathcal{B} and \mathcal{S} denote the set of buses equipped with ES and PV systems respectively, and $\bar{Q}_{\text{solar},i}$ is limited to a fraction of the installed real power capacity of the solar generation. Constraints (12f)–(12h) define the limits on bus voltages, line currents, and generation capacities for the generation units. The ES charge and discharge rates are also bounded by their respective maximum capacities, as shown in equation (12i), where N_i^{ES} represents the integer number of ES units installed at bus i , with $\mathbb{Z}_{\geq 0}$ denoting the set of all positive integers including zero.

Finally, the ES dynamics are modeled to capture the evolution of the SoC of ES units over time. The constraints (12k) govern the charging and discharging behavior of the ES units, with η_i^{ch} and η_i^{dis} representing the charging and discharging efficiencies of the units. This formulation also ensures the cycling behavior of the battery energy state across time steps through (12j), which enforces that the starting and ending SoC of each ES is the same for each operational period. This is particularly useful in planning studies where periodic operation is assumed. To reflect discrete ES sizing decisions, the energy capacity constraint for each ES unit is given by the final constraint (12l), where \bar{E}^{unit} is the rated energy capacity (in MWh) of a single ES unit. The reactive power capacity of the ES units is also constrained in a similar fashion.

Outer Planning Problem: At the second level, we address the planning problem, which determines long-term infrastructure investment decisions. In this formulation, we do not model individual generators explicitly at each bus; instead, we represent them collectively through a coupling term

that captures the exchange with the external grid. While including individual generators would only alter the associated cost term (without changing the underlying problem structure), for the sake of clarity in the case study presented later, we adopt the coupling-based representation. The coupling cost, denoted by C_{coupling} , depends on the installed external grid capacity required during the entire operational horizon. It is determined by the maximum, taken across all time steps, of the total generation from all buses with grid-connected generators. In other words, we consider the largest instantaneous demand for external coupling that occurs during the planning horizon.

The planning objective accounts for three investment decisions: (i) the installation of solar capacity, priced at C_{solar} per unit; (ii) the deployment of ES units, each costing C_{batt} ; and (iii) the required extent of external grid coupling, priced at C_{coupling} per unit of coupled capacity. The planning period spans \mathcal{P} time steps, and $\mathcal{J}_{\text{operational}}$ denotes the solution to the operational-level problem described above. With these definitions, the final planning problem is formulated as:

$$\mathcal{J}_{\text{planning}} = \min \left\{ C_{\text{solar}} \sum_{i \in \mathcal{S}} P_{\text{solar},i} + C_{\text{batt}} \sum_{i \in \mathcal{B}} N_i^{\text{ES}} + C_{\text{coupling}} \sum_{i \in \mathcal{N}} \sum_{g \in \mathcal{G}_i} \left(\max_{t \in \mathcal{T}_n} P_g^{(t)} \right) + \mathcal{P} \cdot \mathcal{J}_{\text{operational}} \right\}. \quad (14)$$

Thus, this planning objective specifies a microgrid configuration in which the individual components are optimally sized and operated to reliably meet demand throughout the planning horizon, while ensuring that all operational constraints of the grid are continuously satisfied.

5.2. Energy Storage Siting

While the sizing problem in Section 5.1 decides how much storage capacity should be allocated based on the demand profiles, the selection of the buses where ES units are located is governed by a separate ES siting or placement optimization problem. Before formulating the placement problem, it is important to understand the underlying motivation. In this network, ES units serve multiple roles: in addition to storing surplus energy for use during generation shortfalls, they function as dynamic sources and sinks of reactive power, thus playing a key role in maintaining voltage stability across the grid. Maintaining optimal voltage conditions is essential for the proper functioning of all loads and grid components. However, the consumption of reactive power exhibits spatiotemporal variations that depend on the traffic patterns across the cells connected to each bus. Consequently, the strategic placement of ES units must reflect this distribution, ensuring reactive power support is available where and when it is most needed. Proper placement enables the grid to respond adaptively to dynamic traffic conditions, enhancing voltage regulation and overall system resilience.

The objective of the ES placement problem is to identify the set of buses best suited for installing ES units. The formulation iteratively varies the number of available units, yielding an optimal siting configuration for each case. This process continues until a preferred number of units and a corresponding placement pattern are found that best enhance system reliability and efficiency. The focus here is solely on siting, while sizing decisions, that is, the number of units and their aggregate energy capacity (MWh) are scenario-dependent and addressed in Section 5.1. For the placement problem, we modify the planning objective in (14) to incorporate binary decision variables and cardinality constraints specific to storage siting. Recall that $N_i^{\text{ES}} \in \mathbb{Z}_{\geq 0}$ denotes an integer that represents the number of storage units installed at bus i . The ES energy capacity at each bus is then constrained as:

$$E_i^{(t)} \leq \bar{E}^{\text{unit}} \cdot N_i^{\text{ES}}. \quad \forall i \in \mathcal{N}, \forall t \in \mathcal{T}_n, \quad (15a)$$

with

$$\sum_{i \in \mathcal{N}} N_i^{\text{ES}} = k_{\text{batt}}, \quad (15b)$$

where $k_{\text{batt}} \in \mathbb{Z}_{>0}$ denotes the total number of ES units available for placement. This results in a Mixed-Integer Linear Program (MILP) that remains non-convex due to the integer battery variable N_i^{ES} . To improve tractability during the initial siting phase, where the focus is on identifying candidate locations rather than determining the number of ES units, the integer constraints on the sizing variable can be relaxed to allow continuous values. This partial relaxation significantly reduces the computational burden and enables more efficient exploration of the solution space. The problem is then solved repeatedly for different values of k_{batt} to determine the optimal number of ES units and their placement configuration. With the results of the placement problem, the system sizing problem in Section 5.1 can then be solved to determine the optimal number and capacity of ES units at the selected buses.

5.3. Algorithmic Implementation

Our overall framework for DWC grid planning, presented in Algorithm 1, builds on the sizing and siting optimization problems in Sections 5.1 and 5.2. We first solve the siting problem in 5.2 to obtain the locations at which ES is placed. We then solve the microgrid sizing problem in Section 5.1 with these ES locations fixed under a variety of traffic scenarios (traffic flows, capacity reductions, ramp flows) and average the resulting solar and ES sizes to obtain the final microgrid design. We will later validate this algorithm through case studies in Sections 6 and 7.

Algorithm 1 Traffic-Aware DWC Microgrid Planning Framework

Input: Roadway segment with N cells and parameters $(v_{ff,i}, w_i, q_{cap,i}, \rho_{crit,i}, \rho_{jam,i})$ for each cell $i \in \{1, 2, \dots, N\}$, on- and off-ramp flows, battery parameters $SoC_{mile}, E_{battery}$, drive power parameters $\eta_{drive}, C_d, C_{rr}, A, m, \rho_{air}, P_{aux}, g$, planning horizon \mathcal{P}

Output: Optimal microgrid parameters (solar and ES capacities $P_{solar,i}, i \in \mathcal{S}$, $N_i^{ES}, i \in \mathcal{B}$ and ES locations \mathcal{B})

Step 1: Traffic Modeling and Demand Estimation

- 1: Select roadway segment and collect traffic and ramp data
- 2: Simulate the CTM to obtain vehicle densities over time using the CTM in (2)-(7)
- 3: Compute energy demand using the energy consumption model in (11)

Step 2: ES Placement Optimization

- 4: Determine optimal ES placement by solving the planning problem with
- 5: objective $\mathcal{J}_{\text{planning}}$ in (14) subject to constraints (12) and (15) for
- 6: various k_{batt} to identify candidate buses for ES placement

Step 3: Scenario Generation and Simulation

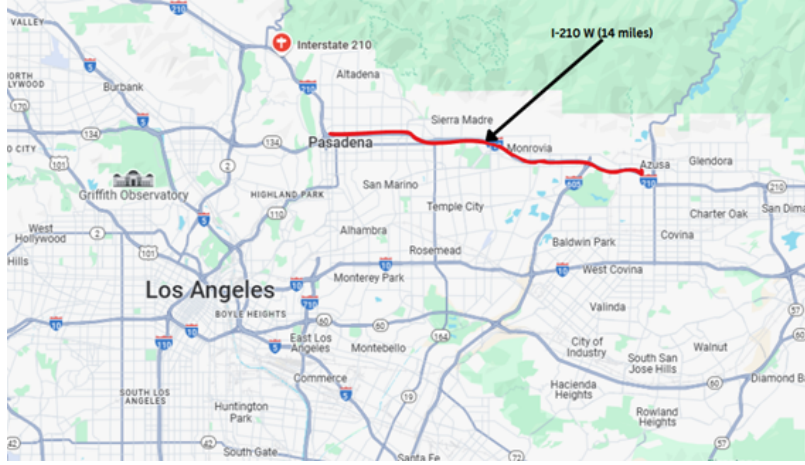
- 7: **for** $s = 1$ to $N_{\text{scenarios}}$ **do**
- 8: Generate traffic scenario s (normal variations, accidents, construction and forest fires)
- 9: Simulate traffic dynamics and update energy demand using Step 1 (lines 1-3)
- 10: Re-optimize the planning objective $\mathcal{J}_{\text{planning}}$ in (14) with constraints (12) and ES locations fixed from Step 2 (line 4)
- 11: Record resulting design parameters for scenario s
- 12: **end for**

Step 4: Final Design and Validation

- 13: Average the $P_{solar,i}$ and N_i^{ES} obtained for traffic scenarios s to obtain the final microgrid design
- 14: Fix a threshold ϵ_{serv} for required service level, defined as the percentage of scenarios s for which DWC demands are required to be met
- 15: Validate final design by simulation under all scenarios to compute the percentage of scenarios for which DWC demands are satisfied by the microgrid design, denoted by $\hat{\epsilon}_{\text{serv}}$
- 16: If $\hat{\epsilon}_{\text{serv}} < \epsilon_{\text{serv}}$, increase $P_{solar,i}$ and N_i^{ES} until $\hat{\epsilon}_{\text{serv}} \geq \epsilon_{\text{serv}}$

6. Case Study - Set-Up

We now present the set up of a case study to validate the design framework described in the previous sections. For this case study, we consider a 14-mile segment of the Interstate 210 West (I-210 W) corridor, located near the city of Los Angeles, California, as shown in Fig. 4. This segment begins near Vernon and ends at the junction where I-210 splits from State Route 134 (SR-134). This segment is chosen for three reasons. First, this is one of the major highway segments serving the Greater Los Angeles area, a region that is both densely populated and experiences heavy traffic throughout the day [32]. These characteristics make this segment a representative candidate for evaluating the feasibility of DWC infrastructure on U.S. highways. Second, the I-210 W is also a well-monitored corridor, with traffic data collected daily at regular intervals through the Performance Measurement System (PeMS) maintained by the California Department of Transportation (CalTrans) [33]. The system provides vehicle flow data for most ramps and sections



The two central buses (Buses 0 and 1) form the interface with the external grid and the solar generation units. Among these, one of the central buses (Bus 0) is directly connected to both the external grid and the solar plant. ES units are distributed across the remaining buses, with their placement determined by the ES placement optimization problem (note that the ES unit placements shown in Fig. 5 are for representational purposes only).

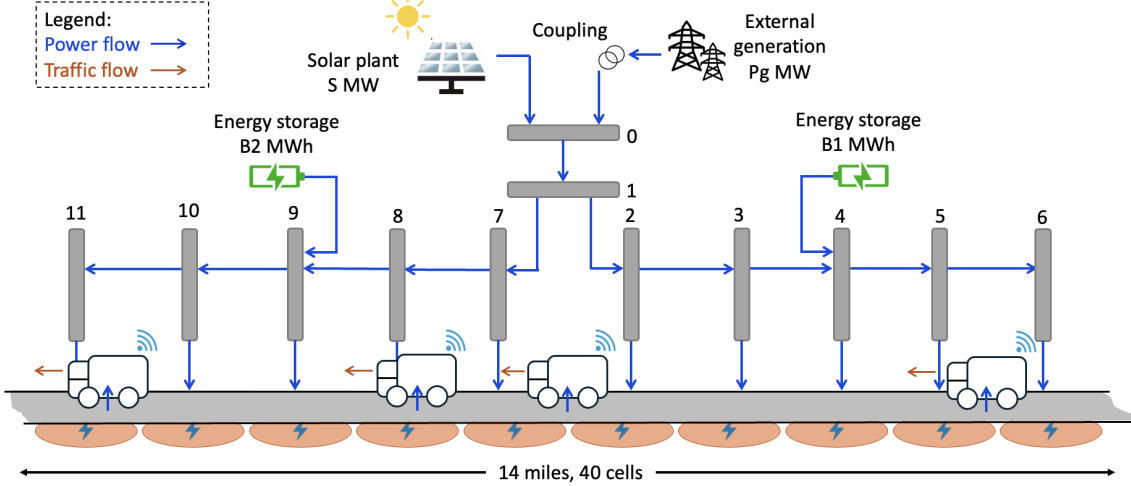


Figure 5: Designed 12-bus microgrid system for the DWC planning problem, incorporating solar generation, ES units, and external grid coupling.

In the grid layout, Buses 0 and 1 are assumed to be separated by a distance of 5 miles. From Bus 1, two branches extend to Buses 2 and 7, each located 2 miles away. All remaining buses in the network are connected sequentially, with a uniform spacing of 1.4 miles between adjacent nodes. The electrical characteristics of the transmission lines, specifically resistance and reactance, vary proportionally with the corresponding line lengths, ensuring a realistic representation of line impedance across the network. The microgrid planning problem is run for a period of 20 years, as defined by the time period in (14).

6.1.1. Traffic Scenarios

The integration of the microgrid design with realistic traffic dynamics forms the core novelty of this work. The key objective is to design a microgrid capable of supporting the DWC system under a wide range of traffic scenarios. Traffic flow on a roadway is inherently unpredictable, influenced by numerous interrelated factors including weather, road conditions, disruptions, and even abstract elements such as human reactions and driving behavior. These uncertainties translate into fluctuations in roadway power demand, appearing as spikes or disruptions in the energy profile. To ensure reliable operation, the proposed grid must be tested against such disturbances, and its parameters must be robust enough to accommodate them without significant performance degradation.

To this end, we generate multiple realistic traffic scenarios that reflect commonly observed events on highways. These scenarios span a spectrum of operating conditions, from routine daily traffic variations to major disruptions caused by accidents or natural disasters. Each scenario is implemented by adjusting specific parameters within the CTMSIM tool, allowing us to capture

how different traffic behaviors impact the corresponding energy demand. We note that formulating such scenarios is non-trivial. Traffic behavior is highly sensitive to the localized nature of events and the real-time reactions of individual drivers. The same disruption can yield widely different outcomes depending on its location, severity, and the surrounding traffic composition. This makes purely analytical prediction difficult. Nevertheless, by identifying broad categories of recurrent highway events, it is possible to construct representative scenarios that, while simplified, capture the essential dynamics of traffic flow and provide a meaningful basis for simulation and system evaluation.

Based on documented traffic events in this region and general highway traffic behavior, we classify the traffic scenarios into four types, each representing a distinct condition or disruption:

- **Normal Variations (NV):** Fluctuations in baseline traffic patterns are caused by regular changes in demand during peak and off-peak hours. These occur throughout the day, with ramp inflows/outflows, initial densities, and demand profiles obtained for each run by adding suitable Gaussian noise to the baseline profile.
- **Construction Work Events (CW):** Planned disruptions due to scheduled roadwork are often preceded by partial on-ramp reductions or speed restrictions before lane closures take effect. These events typically last all day, and are modeled through reduced on- and off-ramp capacities at neighboring cells where the events occur. The density and demand profiles are also varied to assess their impact.
- **Accidents (ACC):** Unplanned incidents disrupting normal traffic operations can be further categorized as:
 - **Mainline:** Accidents on the main highway lanes, typically causing congestion, lane blockages, and significant reductions in traffic flow are classified by severity into *Mild*, *Moderate*, and *Severe* categories, with probabilities of 30%, 30%, and 40%, respectively. Severity is defined by the number of lanes blocked. For each case, nearby on- and off-ramp capacities, as well as initial densities of the cells, are varied to simulate the impact.
 - **Ramp:** Accidents occurring at on-ramps disrupting ramp metering and inflow conditions are generally more localized compared to mainline accidents. The affected on-ramp is closed, and the event duration is randomly selected between 1-3 hours.
- **Natural Disasters like Forest Fires (FF):** High-impact events, including extreme weather conditions and scenarios such as wildfires (particularly relevant in Southern California), that lead to emergency detours, road closures, or evacuation-related traffic surges are modeled as an all-day event, with the highway closed at the West end and upstream flows doubled.

Each event category encompasses multiple scenarios, with parameters adjusted to capture both the nature and severity of the disruption. The scenarios are designed to be diverse yet representative, enabling the microgrid to be evaluated under a comprehensive range of operating conditions. They are generated using a custom MATLAB script that modifies the base CTMSIM configuration files, selecting and adjusting relevant parameters to ensure both variability and realism in the simulated traffic patterns.

The detailed procedure for implementing these scenarios in CTMSIM is provided in the Appendix. In total, 100 scenarios are generated to assess traffic flow under a variety of conditions. Each simulation produces vehicle density values (vehicles per mile) for every cell at each 5-minute

interval, over a 24-hour period. These traffic density outputs are combined with velocity data and processed using (11) to estimate the corresponding energy demand at each cell. This step directly links traffic behavior to the power requirements at each bus, allowing us to quantify how fluctuations in traffic flow translate into variations in demand.

Fig. 6 illustrates the magnitude of these effects, highlighting the sensitivity of network power demands to changing traffic conditions. Notably, some cells exhibit greater variability than others, which can often be attributed to the presence of nearby ramps or recurring disruptions in those locations across multiple scenarios. The first cell, for example, shows several outliers in its boxplot, reflecting the simulated fluctuations in inflows for different scenarios. The absence of a clear linear trend in demand variations across cells is consistent with realistic traffic simulations, where complex interactions and localized events make it difficult to predict patterns that extend uniformly across the entire roadway. Fig. 6 provides an immediate visual context to understand how traffic dynamics shape demand profiles. Ultimately, the designed microgrid must be able to accommodate these variations, as they are directly reflected in the resulting demand profile.

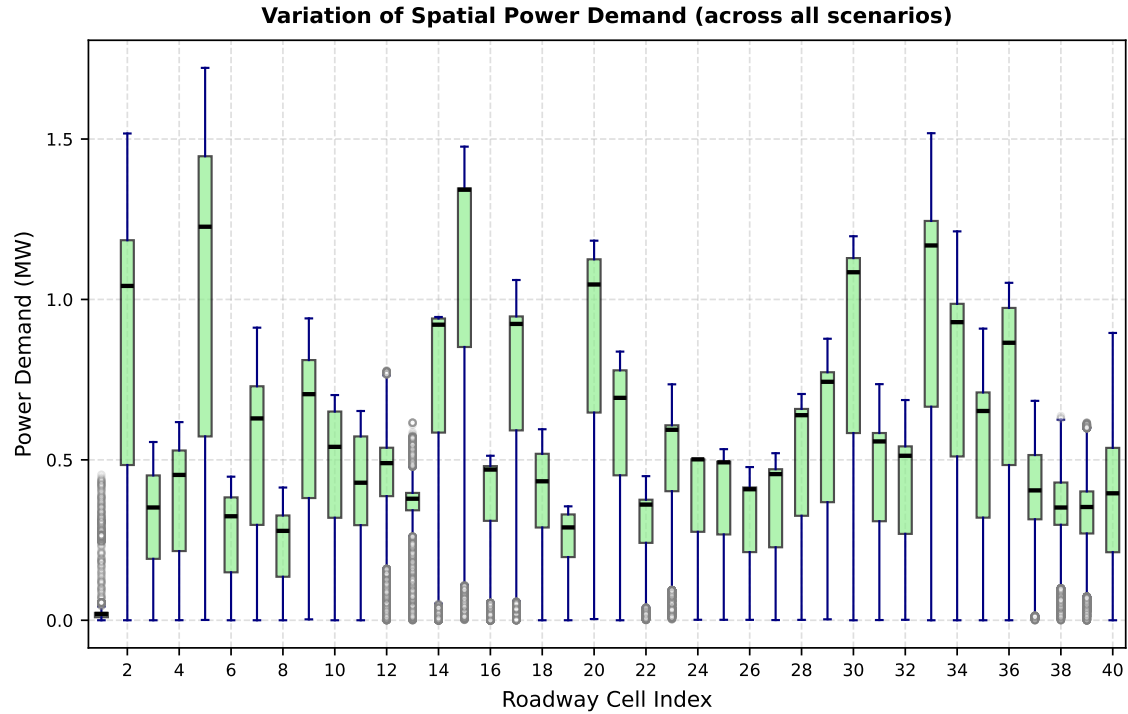


Figure 6: Variation of traffic-induced demand across roadway cells under different simulated traffic scenarios **Boxplot Guide:** Whiskers represent the minimum and maximum demand values (or $1.5 \times$ interquartile range, IQR); the box spans from the 25th to the 75th percentile; and the line inside the box indicates the median demand (50th percentile).

6.2. Dataset Description

The case study is presented through multiple simulations of traffic flow scenarios and their corresponding grid characteristics. As it lies at the intersection of traffic modeling and microgrid

planning, the study requires diverse datasets from different sources. Below is a brief description of the datasets used in this work:

1. **Vehicle Parameters:** This case study focuses on heavy-duty electric trucks (HEVs) in traffic flow modeling, specifically Class 9 vehicles (typical five-axle tractor-semitrailers) as defined by the U.S. Federal Highway Administration [35]. We choose HEVs for this study as they are expected to be among the primary users of DWC on highways [36]. However, it is important to note that this modeling framework can be readily extended to other vehicle classes by adjusting the corresponding parameter values.

We assume that only one lane (the rightmost-lane) is equipped with charging coils. This configuration follows the design proposed in Haddad et. al. [31]. Since direct statistics on the share of HEVs in overall traffic are not available, we assume that all trucks are electric to support a forward-looking and robust infrastructure planning assessment. Based on multiple data sources, trucks account for about 12% of total roadway traffic [37]. It is further assumed that 90% of HEVs operate in the rightmost lane, providing them continuous access to the DWC system [38]. The traffic density values obtained from the CTM are then scaled accordingly to represent HEV density in the rightmost lane. The dynamic energy consumption is modeled using (8)–(11), with parameters defined specifically for HEVs based on the formulations in [36, 39], as summarized in Table A.2 in the Appendix.

2. **CTM Traffic Data:** The CTM traffic data providing realistic traffic flow patterns and densities for the selected segment of I-210 W are derived from the CTMSIM toolbox, which includes a well-calibrated dataset for this corridor. The datasets are based on representative days of the year that capture typical traffic conditions. To test the robustness of the proposed model, multiple realistic traffic scenarios are generated by modulating these base datasets as described in Section 6.1.1.
3. **Solar Generation:** Estimating the installed solar capacity for the microgrid is inherently challenging, as solar plants typically operate at a fraction of their nameplate capacity. This fraction depends on several factors, including geographic location, weather patterns, and seasonal variations. While modeling daily variability is beyond our scope, we used normalized generation data from an 80 MW solar plant in California, sourced from the National Renewable Energy Laboratory (NREL) Grid Modernization synthetic solar PV power plant dataset [40]. The data, averaged over an entire year, provides a representative solar generation profile to support robust microgrid planning.
4. **Microgrid Capital and Operational Costs:** The operational costs correspond to the cost coefficients of power imported from the external grid, as described in Section 3. These parameters are derived from the Texas A&M Grid Repository's 10,000-bus synthetic grid representing the Western U.S. region [41]. The values have been adjusted for inflation and modified to reflect current locational marginal prices (LMPs) in the region.

Capital costs include expenditures related to the installation of the solar plant, individual ES units, and the coupling of the microgrid to the main grid. For solar generation, cost estimates are derived from NREL's 2023 U.S. Solar Photovoltaic System and Energy Storage Cost Benchmark Report [42], which provides a representative figure of approximately 1.17 million USD per installed MW. The cost and technical specifications of the ES units are based on the Tesla Megapack, a utility-scale storage system priced at 960,000 USD for every 3.9 MWh of

capacity [43]. In addition, installation and labor costs are estimated at approximately 240,000 USD per unit [44], bringing the total installed cost to about 1,200,000 USD per ES unit.

The cost of coupling the microgrid to the main grid is more complex to estimate, as it depends on existing grid infrastructure, regional labor rates, and local component costs. In this work, values are drawn from the 2018 Microgrid Planning Study conducted by NREL [45], which includes controls, supporting infrastructure, conventional backup generation, and soft costs. This yields an approximate coupling cost of 1.8 million USD per MW of capacity, after adjustment for inflation. All costs are inclusive of associated transmission infrastructure.

5. **Transmission Line Parameters:** The transmission line parameters primarily depend on the conductor material and its per-unit electrical characteristics, such as AC resistance and reactance. We compute these values by multiplying the per-mile resistance and reactance with the distance between connected buses. The material properties are based on standard values provided in Power System Analysis by Grainger and Stevenson [46]. The conductor type selected is Osprey, a commonly used Aluminum Conductor Steel Reinforced (ACSR) line. The corresponding resistance and reactance values are 0.1679 ohms/mile and 0.432 ohms/mile, respectively. These values are used to calculate the line parameters for all bus-to-bus connections in the microgrid model.

7. Case Study - Results

With the case study established, the next step is to solve the microgrid planning problem and validate it across different traffic scenarios. This case study highlights a strategically important highway segment in the US, providing realistic data that can serve as a foundation for similar studies adopting our framework. The following subsections present the results of individual runs and analyses based on Algorithm 1, defined earlier. We begin by generating the demand pattern for the case study using the default traffic data from CTMSim, followed by the cases corresponding to the traffic scenarios defined in Section 6.1.1.

7.1. Dynamic Energy Consumption

The dynamic energy consumption model provides the key coupling between traffic flow and the corresponding energy demand for the DWC coils. Realistic estimates of traffic conditions at each spatiotemporal point along the roadway are used to compute the aggregate energy demand over time. This establishes a direct connection between transportation dynamics and energy consumption, which in turn informs microgrid design and system sizing. In the long run, monitoring traffic patterns over extended periods allows for the development of statistical bounds on roadway usage, enabling robust estimates of coil-level energy demand fluctuations. While there exists a general proportional relation between traffic density and aggregate energy demand under free-flow or normal variations (which dominate most of the operational period), this relationship breaks down during periods of fluctuating congestion. The nonlinearity arises from the underlying energy consumption model detailed in Section 4.2, where the instantaneous driving power, p_{drive} , is a function of both traffic density and velocity, the latter raised to the third power. Again, since traffic density and velocity are coupled via the CTM and both influence energy consumption, the relationship between density and energy demand becomes inherently nonlinear.

Fig. 7 illustrates the relationship between traffic density and aggregate energy consumption obtained from Step 1 of Algorithm 1 for one of the baseline datasets in CTMSIM. There is a strong

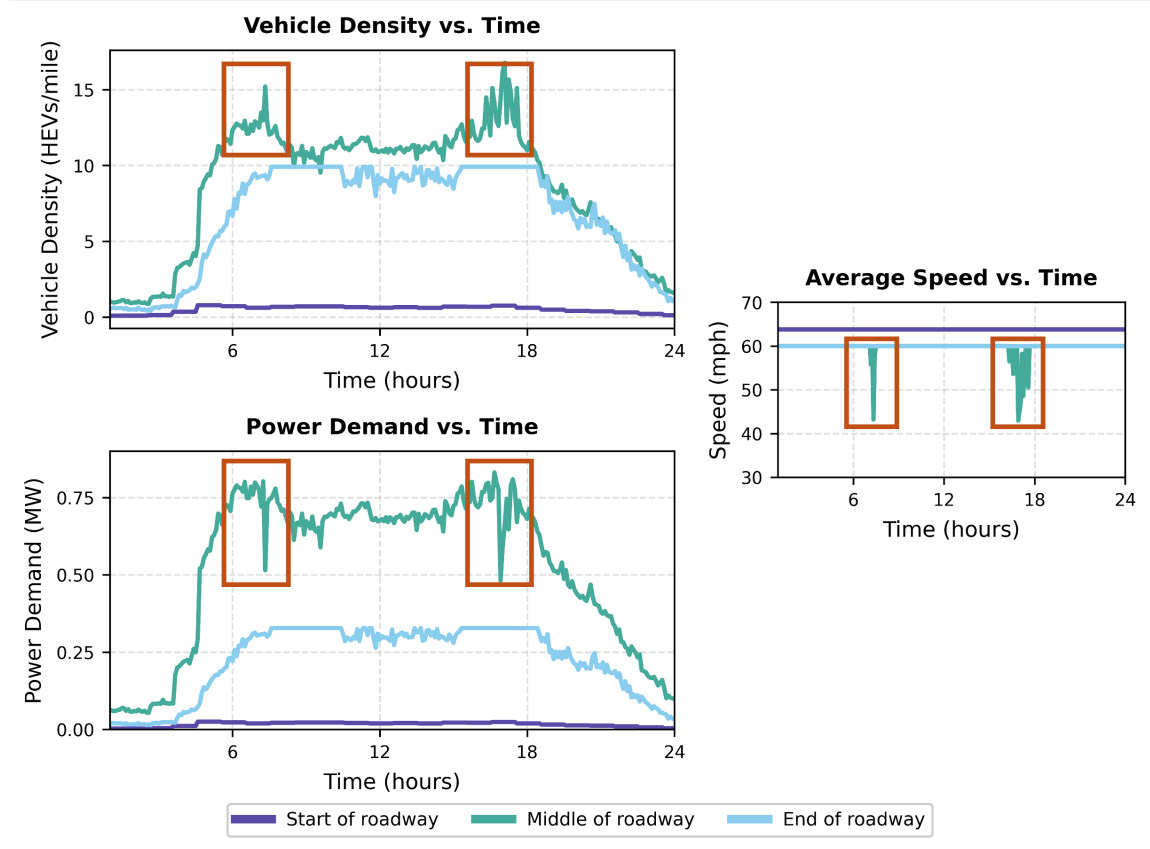
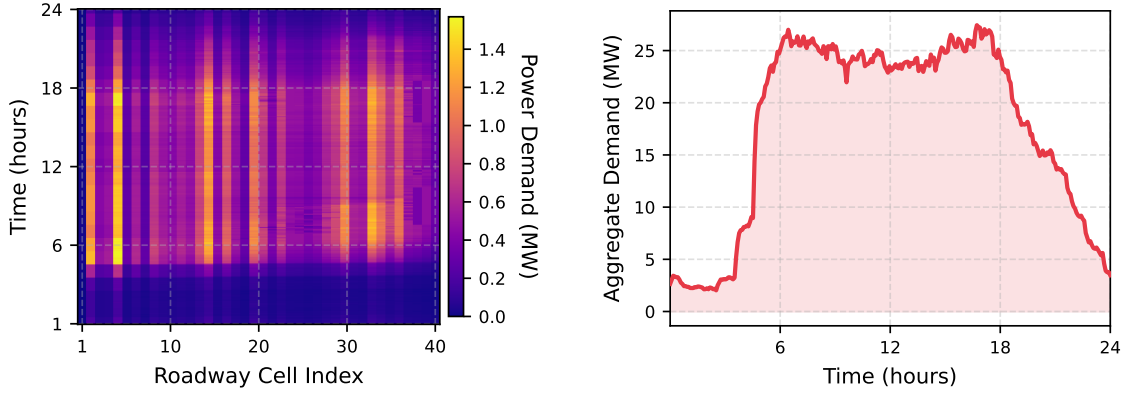


Figure 7: Graphs illustrating vehicle density, power demand, and their nonlinear dependence on average speed for HEVs, with representative cells from the start, middle, and end of the selected roadway segment.

correlation between HEV density and roadway power demand. To show that this pattern holds along the highway, we analyze representative cells from the beginning, middle, and end of the segment over a 24-hour period. Each of these cells displays distinct density and velocity profiles shaped by the nearby on-ramp and off-ramp flows, which in turn drive local energy demand. In general, higher traffic density as shown in the vehicle density vs. time plot in Fig. 7 leads to higher total power demand (power demand vs. time plot in Fig. 7), since more vehicles draw energy from the DWC coils. However, we also observe deviations from this trend where density spikes are accompanied by a drop in power demand. Two such cases are highlighted in the figure. These instances arise due to the impact of traffic congestion, where vehicle speeds fall sharply. Because per-vehicle power demand depends on both density and velocity, lower speeds during congestion reduce total energy consumption, as previously defined by equation 8. The average speed vs. time plot in Fig. 7 supports this notion, showing steep declines in average velocity at the same times as the density spikes.

Fig. 8(a) provides a detailed view of the spatiotemporal demand profile for the roadway segment, illustrating how demand varies across both cells and time periods. Variations in traffic flow, resulting



(a) Spatiotemporal distribution of traffic-driven energy demand along the roadway.

(b) Cumulative energy demand across all roadway cells during the operational period.

Figure 8: Traffic demand from the roadway segment, and its distribution across spatial and temporal scales.

from changes in vehicle density, correspond to fluctuations in the demand profile, as indicated by differences in color intensity. This figure expands upon the demand profile shown in Fig. 7, which focused on representative cells, by displaying demand for all cells along the highway segment. The heatmap demonstrates that demand varies not only over time but also across different locations on the roadway, distinguishing it from conventional static EV charging demand, which only varies temporally. This locational variation in generated demand is precisely what our system design aims to capture. The resulting spatiotemporal demand profile then serves as the input for the microgrid sizing problem.

The graph in Fig. 8(b) shows the cumulative demand for the grid, obtained by summing the demand across all cells at each timestep. For this roadway segment, the maximum demand reaches approximately 27.8 MW. The observed non-linear relationship between traffic flow and energy consumption once again highlights the importance of accurately modeling traffic dynamics to improve energy demand estimation. This demand profile serves as the foundation for the microgrid design presented in the following sections.

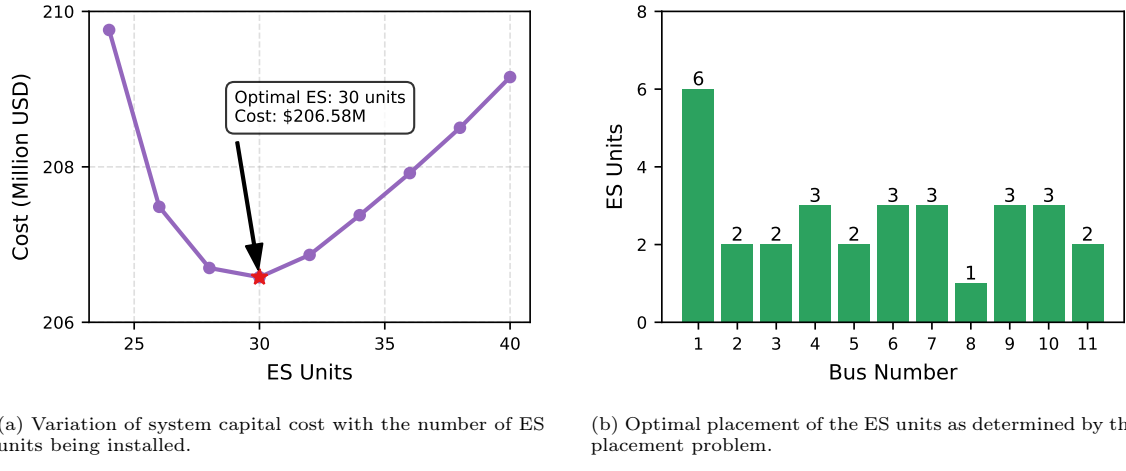
7.2. Grid Planning

Once the load curves for the roadway segment have been obtained, the next step of the overall problem is grid planning. Broadly, this planning task can be divided into two stages: first, the placement of ES units, and second, the sizing of the system based on the identified buses equipped with ES units.

7.2.1. ES Placement

Before proceeding with the sizing of the microgrid, we first need to identify the optimal buses for installing ES units. The purpose of ES placement is to provide effective reactive power support, especially at locations where voltage drops occur due to traffic variations. This corresponds to Step 2 of Algorithm 1. The placement problem is addressed by incrementally varying the total number of ES units k_{batt} in the system. For each configuration, the corresponding total system cost is evaluated, and the configuration with the lowest cost is identified as optimal. Fig. 9(a) illustrates

how the total system cost evolves with the number of ES units. The results indicate that the optimal configuration includes 30 ES units, which minimizes the overall cost. The figure highlights the inherent trade-off between the flexibility introduced by adding ES and the associated installation costs. While ES units reduce the grid's operational costs through their low-cost operation and ability to enhance system flexibility, beyond a certain point their capital costs begin to outweigh these benefits. In our case, this balance establishes 30 units as the cost-effective “sweet spot” for deployment.



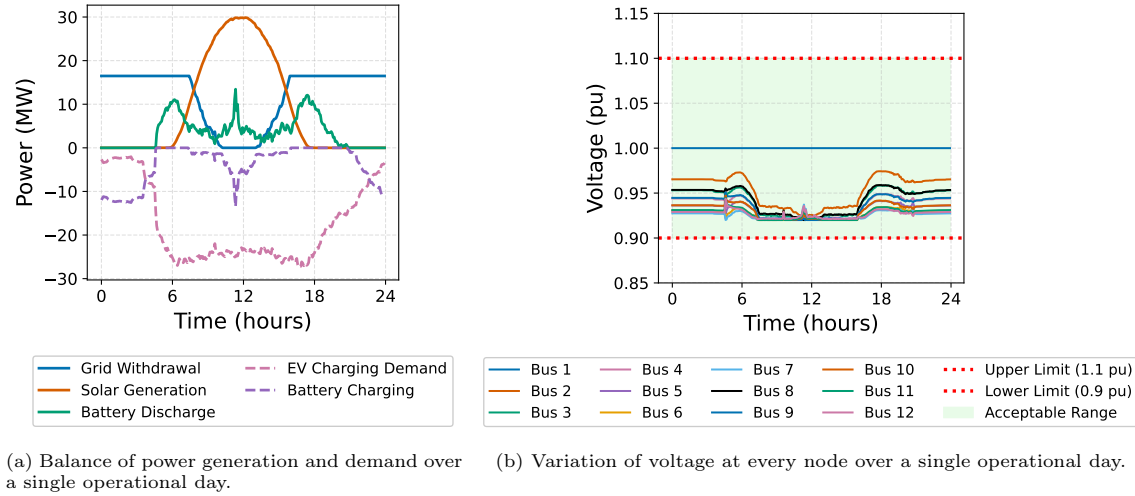
(a) Variation of system capital cost with the number of ES units being installed.

(b) Optimal placement of the ES units as determined by the placement problem.

Figure 9: Results for the ES placement optimization illustrating how varying the number of ES units affects the planned microgrid's total cost.

Once the lowest-cost configuration is identified, we examine the corresponding distribution of ES units across the system. At this stage, the specific storage capacity allocated to each bus is not considered, as it depends on the demand profile. Instead, we focus on a representative case that provides the optimal placement locations for ES units. These placements are determined based on their ability to maintain system voltages within limits by supplying or absorbing reactive power as codified in constraints (12d)-(12f). The corresponding distribution of ES units across the buses is shown in Fig. 9(b). Based on the radial grid structure shown in Fig. 5, Bus 0 is excluded from ES installation in the optimized solution as its greater electrical distance from the other buses leads to higher transmission losses when supporting the grid, thereby increasing overall system cost. In contrast, Bus 1 occupies a more central position and is therefore the most favorable location for installation, receiving the largest share of ES units. The remaining units are almost uniformly distributed across other buses that serve the highway cells, with slight variations in allocation. These deviations are primarily influenced by the load at each bus under the given demand profile of the DWC coils. For the remaining analysis, ES units are fixed in the configuration of Fig. 9(b).

7.2.2. Microgrid Parameters for Baseline Traffic Flows



(a) Balance of power generation and demand over a single operational day. (b) Variation of voltage at every node over a single operational day.

Figure 10: Baseline traffic flow simulation results showing the variation of generated power by the microgrid components and the voltage profile of the different buses.

The demand profile for the baseline case, previously shown in Fig. 8, illustrates the spatiotemporal demand distribution of the highway DWC load. This distribution serves as the foundation for the subsequent microgrid planning. Solving the sizing problem in Step 3 of Algorithm 1 yields the optimal system parameters for the microgrid, as shown in Fig. 10(a). The results indicate an optimal solar capacity of 43.41 MW and a total ES capacity of approximately 117 MWh. The system also requires a connection to the external grid of about 16.36 MW to ensure reliability during peak demand periods. The total system cost accounts for both the estimated capital cost of construction and the operational cost of grid withdrawals over the 20-year planning horizon.

The graphs in Fig. 10(a) provide a deeper insight into the daily operation of the system. The microgrid power balance curve illustrates the interaction between solar generation, ES units, and external grid withdrawals in meeting the demand. Solar generation peaks around midday, at which point grid withdrawals drop to nearly zero. Any excess solar power is used to charge the ES units, which subsequently discharge during the evening peak when solar generation declines. External grid withdrawals fill in any remaining gaps when neither solar nor ES can fully meet the demand. This behavior aligns with expected system operation. It is important to note that the ES charging and discharging shown in the graph represent the cumulative sum across all ES units.

Fig. 10(b) depicts the voltage profiles for all buses in the system over the operational period. Voltages remain within the acceptable limits, demonstrating that the system is effectively designed to accommodate spatiotemporal demand fluctuations. Minor voltage drops are observed during periods of high demand, which are subsequently mitigated by reactive power supplied from the solar inverters and the strategic placement of ES units. This concludes the system design for the baseline traffic conditions. A similar strategy is then applied to define the microgrid design parameters for each traffic scenario discussed in Section 6.1.1.

7.2.3. Traffic Scenario Simulations

The traffic scenario simulations translate the exhaustive list of scenarios generated in Section 6.1.1 into their corresponding impacts on microgrid parameters. The objective is to understand how varying traffic conditions affect system design, cost, and robustness. These simulations capture the non-linear relationship between traffic flow fluctuations, their resulting energy demand profiles, and the corresponding effects on microgrid sizing obtained from Step 3 of Algorithm 1.

A total of 100 traffic scenarios are simulated, including NV (30 runs), CW (20 runs), ACC-Ramp (5 runs), ACC-Mainline (30 runs), and FF (15 runs). The results are shown in Fig. 11. Each scenario affects traffic flow differently, which in turn alters the energy demand profile and the resulting grid parameters. In contrast to the NV scenario, ACC, CW, or FF often create localized blockages. In these cases, high traffic density in one area is typically offset by reduced density or near-congestion speeds elsewhere, moderating the overall energy demand. This highlights the strong spatiotemporal and non-linear nature of traffic-grid coupling and its influence on system design. Contrary to intuitive expectations, traffic jams and accidents do not always impose the highest system costs; rather, a linear increase in overall traffic flow has a more pronounced impact on microgrid sizing and cost in comparison.

We also examine the impact of these scenarios on the allocations of individual microgrid components as shown in Fig. 11. The results indicate that the optimal solar capacity remains relatively stable across scenarios, with a slight increase under the NV scenarios. This is because solar capacity has the lowest capital cost, reflected in the optimization solution being more weighted towards this resource. However, it is constrained by its limited availability, as determined by the solar generation profile in (12b), which creates a tradeoff beyond a certain point. The system shows the least reliance on external grid coupling. Although the external grid provides a stable supply, the high cost of interconnection and operation keeps its allocation consistently lower across scenarios. The greatest variation is observed in the ES units, which have a mid-range cost and greater flexibility. Their ability to be distributed across any bus in the network allows the system to adapt to varying traffic-driven energy demands. Using these parameters, the next step is to finalize and validate the system design for the proposed grid for different load profiles.

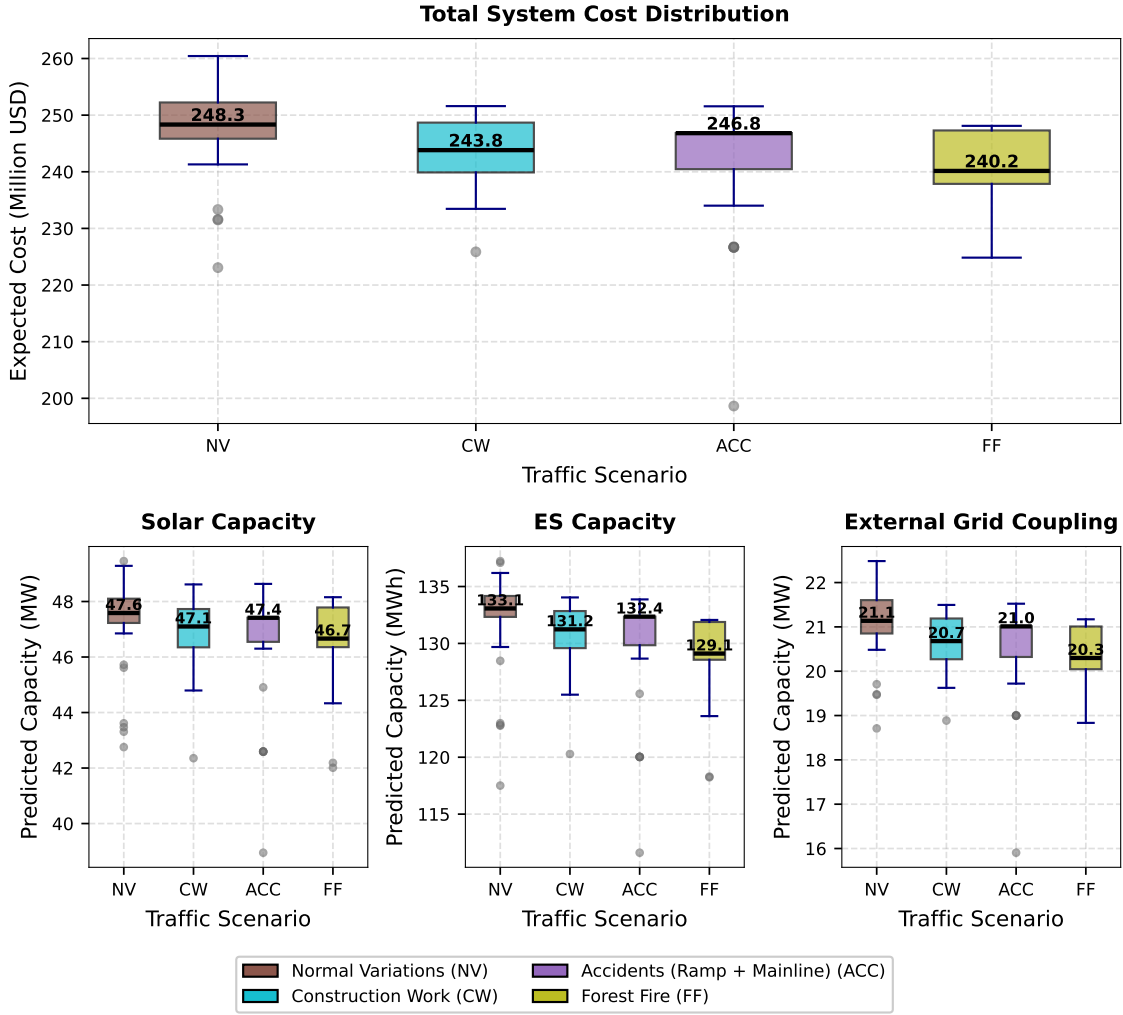


Figure 11: Influence of different traffic scenario types on total system cost and optimal sizing of solar capacity, ES, and external grid coupling.

7.3. Final Microgrid Design and Validation

We conclude by validating the designed microgrid under varying load conditions as discussed in Step 4 of Algorithm 1, constituting the final part of the case study. In Section 7.2.3 we discussed how the different types of traffic scenarios have a direct impact on the microgrid parameters. From Fig. 11, it can be seen that the higher end of the parameter sizes occurs during incremental normal variations of traffic, with the highest mean values also under that category. Thus, to determine a system size that can cater to all traffic scenarios, we consider the one with the highest parameter sizes, which in this case is the NV type, and set the final values for solar, total ES capacity, and external grid coupling to be the mean of all parameters obtained for this scenario type. While a deeper analysis could further refine an optimized system size that may be a better fit across all

traffic scenarios, in the longer run (for example, over the 20-year operational period considered here), a slight variation in sizing has very little direct impact on overall system cost. For this reason, we simply use the average component sizes corresponding to the most demanding traffic scenario type. From the Fig. 11, this corresponds to a 47.6 MW solar plant, 133.1 MWh of total installed ES, and an external grid coupling of 21.1 MW. To determine the distribution of ES across the buses, we refer to the scenario runs from Section 7.2.3, selecting capacities closest to the mean values under the NV cases. This results in the distribution shown in Table 1. As in most cases, Bus 0 is free of ES units, while Bus 1, being the central bus, receives the highest allotment. The remaining buses share a roughly equal distribution of ES capacities.

Table 1: Final distribution of ES capacities across the different buses in the proposed system from Fig. 5.

Bus Index	0	1	2	3	4	5	6	7	8	9	10	11
Predicted ES Capacity (MWh)	0	31.1	11.7	12.2	8.6	11.3	8.1	9.3	8.6	10.8	15.0	6.6

For the validation runs, solving the full AC-OPF in (12) for all possible demand scenarios is impractical. Instead, we simplify the problem to minimize a dummy objective (e.g., a constant) with the real-power balance constraint in (12b) to validate that generated power remains greater than the net demand at every time step across all 100 traffic scenarios. Our validation studies confirm that the system is 100% compliant across all traffic scenarios ($\hat{\epsilon}_{serv} = 100\%$), even though the system size is significantly smaller than that obtained by considering the worst-case demand at every time step, as will be seen in Section 7.4. This not only reduces resource requirements substantially, but also results in a robust, traffic-aware design capable of meeting demand under realistic roadway conditions.

7.4. Cost Comparison With and Without Traffic-Aware Grid Planning

Throughout this work, we have emphasized the importance of coupling traffic flow models with the grid planning problem, showing how the unique operational characteristics of DWC systems can significantly impact system design. With the grid modeling for our case study now complete, we can quantify this impact by comparing the grid costs obtained for our design with that where the traffic flow is assumed to be the worst-case scenario for the roadway segment. We note that we could also compare the costs of our microgrid design with respect to a grid designed to serve the average rather than worst-case demand (with slightly lower associated costs). However, the system designed for the average demand profile will by definition be incapable of meeting the demand under extreme or varying scenarios as it does not account for spatiotemporal demand patterns. Our motivating example in Section 2 illustrates this problem. Thus, we focus the comparison in this section to the worst-case design.

For this comparison, we use the baseline dataset from CTMSIM, which was also used in Section 7.2.2. From the load profile in Fig. 8(b), the load profile peaks at approximately 27.8 MW, corresponding to a maximum energy demand of 2287 kWh on the charging coils (across a 5 minute timestep). In the absence of traffic modeling or spatiotemporal demand variations, we assume a flat load profile with a constant 27.8 MW throughout the day, yielding a worst-case microgrid design capable of sustaining this maximum load at all times. In the traffic-aware case, consistent with our approach of accounting for demand variations due to traffic flow, we use the actual spatiotemporal demand profile shown in Fig. 8(b). This captures realistic fluctuations in demand driven by traffic dynamics, providing a more accurate representation of the system’s energy requirements over time.

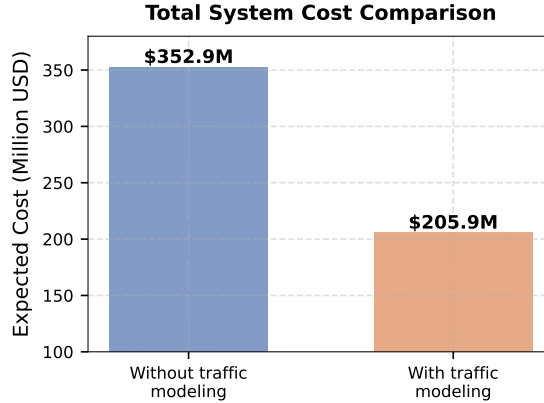


Figure 12: Effect of traffic-aware grid planning on total system cost.

As shown in Fig. 12, ignoring traffic-aware modeling and using a worst-case flat load profile leads to a significant overestimation of system costs. The total cost rises from approximately \$205.9 million in the traffic-aware case to about \$352.9 million when traffic dynamics are ignored, representing a 70% increase. This difference in system sizing extends to every component of the proposed microgrid, as shown in Fig. 13. When traffic flow is ignored, the optimal solar capacity increases from 42.02 MW to 61.84 MW, representing a 47% rise. Similarly, the ES capacity grows from 117 MWh to 188 MWh, a 60.7% increase, reflecting the additional storage required to buffer against the flat, elevated demand profile. The external grid coupling also rises sharply, from 16.36 MW to 32.25 MW, almost a twofold increase, as the system requires greater backup capacity to reliably meet the unvarying peak load. These results demonstrate that ignoring traffic flow variations effectively leads to oversizing the system across all components, resulting in substantially higher capital and operational costs. While peak traffic demand is important for system sizing, it occurs only briefly during the day and can be managed using a combination of generation resources, such as ES units that store energy during low-demand periods. Traffic-aware planning leverages this flexibility, aligning system design with realistic traffic-driven demand, resulting in a more optimally sized system for DWC operations, significantly reducing overall costs and further reinforcing the utility of our framework.

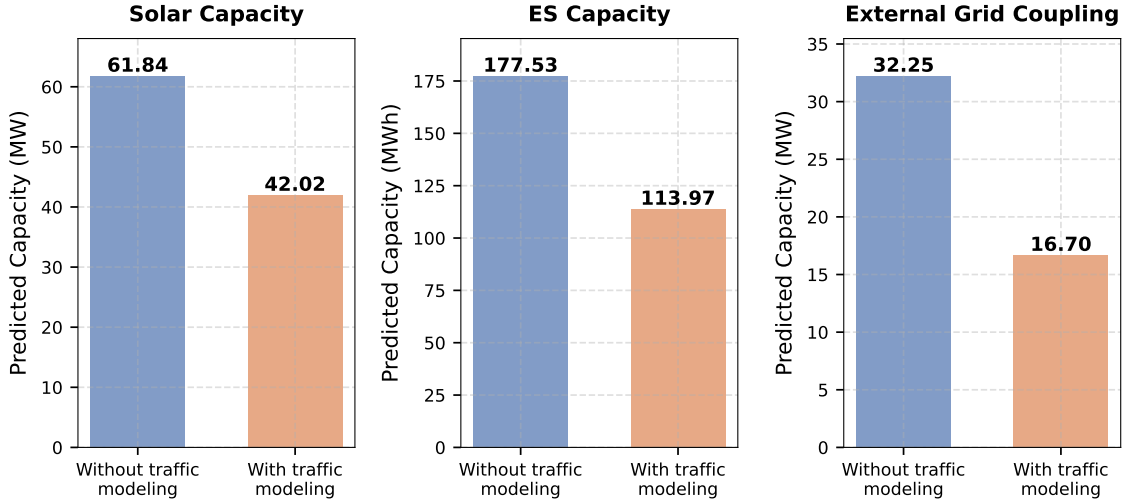


Figure 13: Comparison of optimal solar, ES, and grid coupling capacities in the DWC microgrid with and without traffic-aware modeling.

8. Discussion

In this work, we highlight the challenges associated with one of the emerging EV charging technologies, DWC, particularly in terms of its implementation and integration with the power grid. We introduce the novel idea of linking macroscopic traffic flow dynamics to model roadway energy demand from DWC coils, and then use this model to design a supporting microgrid. We evaluate the robustness of the proposed system across multiple traffic scenarios, with the final design selected to ensure reliable power supply under all load conditions. This coupled traffic–microgrid approach avoids overdesign, saves costs, and eliminates the need for microscopic vehicle-level monitoring, instead relying on informed models capturing average roadway behavior.

A major goal of this work was to develop an adaptive framework that, given sufficient information on historic traffic patterns in a region, can support microgrid planning for DWC installation and operation. The proposed framework provides both the projected system size and corresponding investment requirements, offering stakeholders a practical tool for evaluating and implementing DWC technology along roadways. In doing so, this work not only addresses the technical challenges of integrating DWC into the power grid but also quantifies the economic footprint of the supporting infrastructure. An observation here is that our modeled microgrid parameters are heavily dependent on the assumed system capital and operational costs. While we have incorporated the latest available discretized costs, adjusted for inflation, these parameters can be updated based on the roadway region and the year in which the microgrid is to be constructed. The generalized formulation of our models and optimization framework also allows them to be adapted with market trends and region-specific constraints, making it relevant for a wider audience of planners and investors.

Finally, we leverage spatiotemporal variability of traffic demand to enhance system flexibility. This opens up the potential for our models to be used in demand modeling for ancillary services like demand response. Future work will focus on integrating demand response, enabling market

participation, and advancing traffic models with higher-resolution data, all of which can strengthen the role of DWC in sustainable grid operation.

9. CRediT authorship contribution statement

Dipanjan Ghose - Writing – original draft, Visualization, Validation, Software, Methodology, Data curation, Conceptualization. **S Sivarajani** - Writing – review & editing, Supervision, Resources, Methodology, Funding acquisition, Conceptualization. **Junjie Qin** - Writing – review & editing, Supervision, Resources, Methodology, Funding acquisition, Conceptualization.

10. Declaration of competing interest

The authors declare that they have no known competing financial interests or personal relationships that could have appeared to influence the work reported in this paper.

Appendix A. Traffic Scenario Parameters

Fig. A.14 summarizes how various traffic scenarios are implemented in CTMSIM by varying the input parameters. In terms of nomenclature, OR-max and FR-max refer to the maximum allowable flow rates for on-ramps and off-ramps, respectively. The demand profile corresponds to the input demand values at on-ramps, while the FR-flow profile represents the expected flow rates at off-ramps. Initial densities denote the traffic density in each cell at the start of the simulation. All parameter values were scaled from the original calibrated values provided in CTMSIM to preserve alignment with realistic traffic conditions observed along the I-210 W segment. To obtain the traffic demand variations for the scenarios, we developed a MATLAB script that continuously calls the CTMSIM simulator with updated individual variables, generating new traffic simulation outputs for density and speed at each cell and timestep. These results are then fed into the dynamic energy consumption model to derive the corresponding demand variations.

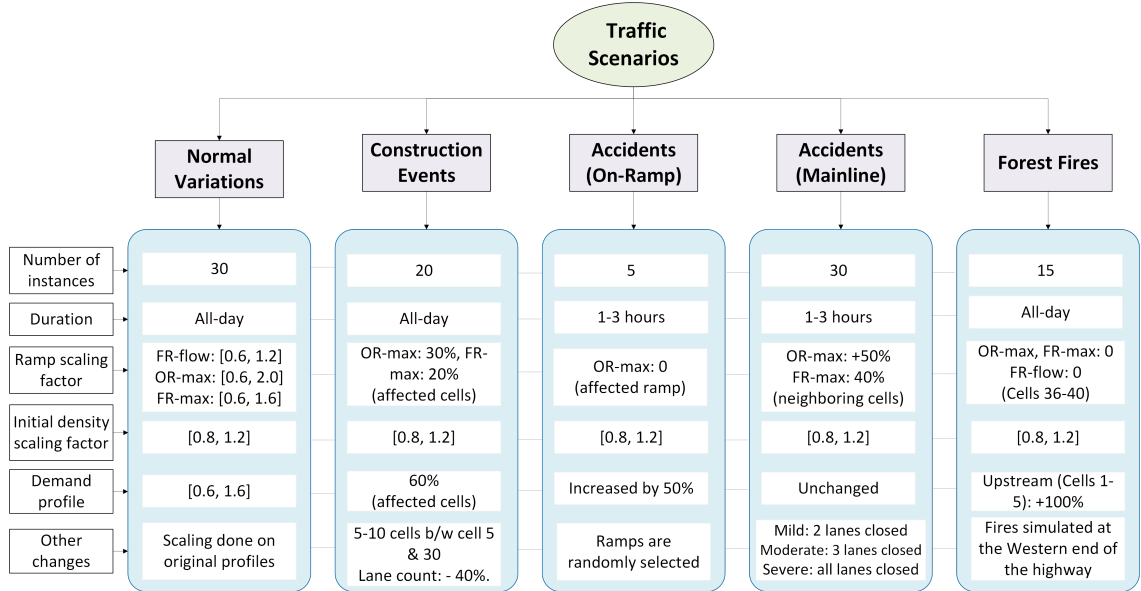


Figure A.14: Scenario description for the CTMSim traffic model

Table A.2 presents the vehicle parameters used to estimate the power consumption of HEVs in our case study [31].

Table A.2: Key parameters for HEVs in the case study.

Parameter	Value
η_{drive}	0.92
C_d	0.65
C_{rr}	0.0068
A	10.2 m ²
ρ_{air}	1.225 kg/m ³
m	30.5 tons
g	9.8 m/s ²
E_{battery}	311 kWh
p_{aux}	7.5 kW
SoC _{mile}	0.15%

References

[1] Z. Ye, M. A. Bragin, N. Yu, R. Wei, Joint planning of dynamic wireless charging lanes and power delivery infrastructure for heavy-duty drayage trucks, *Applied Energy* 375 (2024) 124029. doi:10.1016/j.apenergy.2024.124029.

- [2] J. Shi, H. O. Gao, Efficient energy management of wireless charging roads with energy storage for coupled transportation–power systems, *Applied Energy* 323 (2022) 119619. doi:10.1016/j.apenergy.2022.119619.
- [3] INDOT, Wireless Electric Vehicle Charging Solution for Highway Infrastructure, last Modified: 2022-09-12T19:21:25-04:00 (Aug. 2021).
URL <https://www.in.gov/indot/current-programs/innovative-programs/wireless-electric-vehicle-charging-solution-for-highway-infrastructure/>
- [4] S. Lozanova, Dynamic wireless charging for electric vehicles, accessed: 2025-09-01 (Sep 2025).
URL <https://www.greenlancer.com/post/dynamic-wireless-charging-electric-vehicles>
- [5] V. N. Galigekere, B. Ozpineci, High power and dynamic wireless charging of electric vehicles (evs), Tech. rep., Oak Ridge National Laboratory (ORNL), Oak Ridge, TN (June 2021).
- [6] Electreon, Trondheim electric road project, Web page, first wireless Electric Road System in Norway, planned construction and operation start 2024; accessed October 26, 2025 (2023).
URL <https://electreon.com/projects/trondheim-electric-road-project>
- [7] A. Ferrara, S. Sacone, S. Siri, First-Order Macroscopic Traffic Models, in: A. Ferrara, S. Sacone, S. Siri (Eds.), *Freeway Traffic Modelling and Control*, Springer International Publishing, Cham, 2018, pp. 47–84. doi:10.1007/978-3-319-75961-6_3.
- [8] C. F. Daganzo, The cell transmission model: A dynamic representation of highway traffic consistent with the hydrodynamic theory, *Transportation Research Part B: Methodological* 28 (4) (1994) 269–287.
- [9] S. Lukic, Z. Pantic, Cutting the Cord: Static and Dynamic Inductive Wireless Charging of Electric Vehicles, *IEEE Electrification Magazine* 1 (1) (2013) 57–64. doi:10.1109/MELE.2013.2273228.
- [10] C. Panchal, S. Stegen, J. Lu, Review of static and dynamic wireless electric vehicle charging system, *Engineering Science and Technology, an International Journal* 21 (5) (2018) 922–937. doi:10.1016/j.jestch.2018.06.015.
- [11] A. J. Sauter, J. D. Lara, J. Turk, J. Milford, B.-M. Hodge, Power system operational impacts of electric vehicle dynamic wireless charging, *Applied Energy* 364 (2024) 123002. doi:10.1016/j.apenergy.2024.123002.
- [12] T. Fonseca, L. L. Ferreira, B. Cabral, R. Severino, K. Nweye, D. Ghose, Z. Nagy, EVLearn: extending the cityLearn framework with electric vehicle simulation, *Energy Informatics* 8 (1) (2025) 16. doi:10.1186/s42162-024-00445-w.
- [13] D. Ghose, Studying present and future electric vehicle impacts on the city of austin’s power grid, Master’s thesis, The University of Texas at Austin, master’s Thesis (Apr. 2023).
- [14] S. Liu, D. Z. Wang, Q. Tian, Y. H. Lin, Optimal configuration of dynamic wireless charging facilities considering electric vehicle battery capacity, *Transportation Research Part E* 181 (2024) 103376.

- [15] D. M. Nguyen, M. A. Kishk, M.-S. Alouini, Dynamic charging as a complementary approach in modern EV charging infrastructure, *Scientific Reports* 14 (1) (2024) 5785, publisher: Nature Publishing Group. [doi:10.1038/s41598-024-55863-3](https://doi.org/10.1038/s41598-024-55863-3).
- [16] Y. Wang, M. Ma, S. Liang, Y. Wang, N. Liu, Optimal control strategy for electric vehicle platoons in dynamic wireless charging lane considering charge demand differences, *Physica A: Statistical Mechanics and its Applications* 655 (2024) 130190. [doi:10.1016/j.physa.2024.130190](https://doi.org/10.1016/j.physa.2024.130190).
- [17] M. Majidi, M. Parvania, Dynamic in-motion wireless charging systems: Modelling and coordinated hierarchical operation in distribution systems, *IET Generation, Transmission & Distribution* 18 (20) (2024) 3151–3160. [doi:10.1049/gtd2.13212](https://doi.org/10.1049/gtd2.13212).
- [18] Y. Wang, Y. Zhou, X. Yan, Reliable dynamic wireless charging infrastructure deployment problem for public transport services, *European Journal of Operational Research* 313 (2) (2024) 747–766. [doi:10.1016/j.ejor.2023.08.053](https://doi.org/10.1016/j.ejor.2023.08.053).
- [19] A. O. Elmeligy, E. Elghanam, M. S. Hassan, A. H. Osman, A. A. Shalaby, M. Shaaban, Optimal Planning of Dynamic Wireless Charging Infrastructure for Electric Vehicles, *IEEE Access* 12 (2024) 30661–30673. [doi:10.1109/ACCESS.2024.3365636](https://doi.org/10.1109/ACCESS.2024.3365636).
- [20] H. Ngo, A. Kumar, S. Mishra, Optimal positioning of dynamic wireless charging infrastructure in a road network for battery electric vehicles, *Transportation Research Part D: Transport and Environment* 85 (2020) 102385. [doi:10.1016/j.trd.2020.102385](https://doi.org/10.1016/j.trd.2020.102385).
- [21] A. Zaheer, M. Neath, H. Z. Z. Beh, G. A. Covic, A Dynamic EV Charging System for Slow Moving Traffic Applications, *IEEE Transactions on Transportation Electrification* 3 (2) (2017) 354–369. [doi:10.1109/TTE.2016.2628796](https://doi.org/10.1109/TTE.2016.2628796).
- [22] N. Aung, W. Zhang, K. Sultan, S. Dhelim, Y. Ai, Dynamic traffic congestion pricing and electric vehicle charging management system for the internet of vehicles in smart cities, *Digital Communications and Networks* 7 (4) (2021) 492–504. [doi:10.1016/j.dcan.2021.01.002](https://doi.org/10.1016/j.dcan.2021.01.002).
- [23] I. Karakitsios, E. Karfopoulos, N. Hatzigyriou, Impact of dynamic and static fast inductive charging of electric vehicles on the distribution network, *Electric Power Systems Research* 140 (2016) 107–115.
- [24] R. Sun, Q. Luo, Y. Chen, Optimizing dynamic wireless charging for electric buses: A data-driven approach to infrastructure planning, *Applied Energy* 373 (2024) 123912. [doi:10.1016/j.apenergy.2024.123912](https://doi.org/10.1016/j.apenergy.2024.123912).
- [25] P. Aduama, A. S. Al-Sumaiti, K. H. Al-Hosani, A. R. El-Shamy, Optimizing quasi-dynamic wireless charging for urban electric buses: A two-scenario mathematical framework with grid and PV-battery systems, *Heliyon* 10 (15), publisher: Elsevier (Aug. 2024). [doi:10.1016/j.heliyon.2024.e34857](https://doi.org/10.1016/j.heliyon.2024.e34857).
- [26] M. Majidi, M. Parvania, Spatio-Temporal Impact Analysis of Dynamic Wireless Charging of Electric Vehicles on Power Distribution Systems, in: 2024 18th International Conference on Probabilistic Methods Applied to Power Systems (PMAPS), 2024, pp. 1–6, iSSN: 2642-6757.

[27] M. Farivar, S. H. Low, Branch Flow Model: Relaxations and Convexification—Part I, *IEEE Transactions on Power Systems* 28 (3) (2013) 2554–2564. doi:10.1109/TPWRS.2013.2255317.

[28] F. Alimardani, J. S. Baras, Performance assessment of different cell-transmission models for ramp-metered highway networks, in: IFAC symposium on control in transportation systems, Vol. 54 of IFAC-PapersOnLine, Elsevier, 2021, pp. 114–120, number: 2.

[29] C. F. Daganzo, Traffic density estimation with the cell transmission model, in: Proceedings of the 33rd IEEE Conference on Decision and Control, IEEE, 1994, pp. 2221–2225. doi:10.1109/CDC.1994.1240418.
URL <https://doi.org/10.1109/CDC.1994.1240418>

[30] L. Munoz, X. Sun, D. Sun, G. Gomes, R. Horowitz, Methodological calibration of the cell transmission model, in: Proceedings of the 2004 American Control Conference, Vol. 1, 2004, pp. 798–803 vol.1, iSSN: 0743-1619. doi:10.23919/ACC.2004.1383703.

[31] D. Haddad, T. Konstantinou, D. Aliprantis, K. Gkritza, S. Pekarek, J. Haddock, Analysis of the financial viability of high-powered electric roadways: A case study for the state of Indiana, *Energy Policy* 171 (2022).

[32] AARoads Interstate Guide, Interstate 210 California, <https://www.aaroads.com/interstate-guide/i-210-ca/>, retrieved July 20, 2025 (2018).

[33] California Department of Transportation, Caltrans PeMS, <https://pems.dot.ca.gov/>, retrieved July 20, 2025 (2025).

[34] A. Kurzhanskiy, CTMSIM - an interactive freeway traffic macrosimulator, <https://www.mathworks.com/matlabcentral/fileexchange/21977-ctmsim-an-interactive-freeway-traffic-macrosimulator>, mATLAB Central File Exchange. Retrieved September 6, 2025 (2025).

[35] Federal Highway Administration, Traffic monitoring guide - updated october 2016, accessed: 2025-09-01 (Oct. 2016).
URL <https://rosap.ntl.bts.gov/view/dot/50512>

[36] D. Haddad, T. Konstantinou, D. Aliprantis, K. Gkritza, S. Pekarek, J. Haddock, Analysis of the financial viability of high-powered electric roadways: A case study for the state of Indiana, *Energy Policy* 171, publisher: Elsevier Ltd (Dec. 2022). doi:10.1016/j.enpol.2022.113275.

[37] M. Sivak, States with the highest and lowest truck traffic on interstate highways, <https://www.greencarcongress.com/2021/03/20210316-sivak.html>, blog: Green Car Congress. Sivak Applied Research. Accessed: 2025-07-20 (2021).

[38] California Department of Transportation, Truck lane use, <https://dot.ca.gov/programs/traffic-operations/legal-truck-access/truck-lane-use>, accessed: 2025-07-20 (2025).

[39] I. E. Agency, Global EV outlook 2023: Trends in electric heavy-duty vehicles, Tech. rep., International Energy Agency (2023).
URL <https://www.iea.org/reports/global-ev-outlook-2023/trends-in-electric-heavy-duty-vehicles>

- [40] National Renewable Energy Laboratory (NREL), Solar power data for integration studies, <https://www.nrel.gov/grid/solar-power-data>, retrieved July 21, 2025 (2025).
- [41] Texas A&M University, Electric Grid Test Case Repository, ACTIVSg10k: 10000-bus synthetic grid on footprint of western United States, <https://electricgrids.enr.tamu.edu/electric-grid-test-cases/activsg10k/>, retrieved July 21, 2025 (2025).
- [42] V. Ramasamy, J. Zuboy, M. Woodhouse, E. O'Shaughnessy, D. Feldman, J. Desai, A. Walker, R. Margolis, P. Basore, U.S. Solar Photovoltaic System and Energy Storage Cost Benchmarks, With Minimum Sustainable Price Analysis: Q1 2023, Renewable Energy (2023).
- [43] Tesla, Inc., Megapack – Utility-Scale Energy Storage, <https://www.tesla.com/megapack>, accessed July 21, 2025 (2025).
- [44] Pacific Northwest National Laboratory, Esgc: Energy storage cost and performance, <https://www.pnnl.gov/projects/esgc-cost-performance/lithium-ion-battery>, accessed: 2025-06-02 (2023).
- [45] J. I. Giraldez Miner, F. Flores-Espino, S. MacAlpine, P. Asmus, Phase I Microgrid Cost Study: Data Collection and Analysis of Microgrid Costs in the United States, Tech. rep., National Renewable Energy Laboratory (NREL), Golden, CO (United States) (Oct. 2018). doi:10.2172/1477589.
URL <http://www.osti.gov/servlets/purl/1477589/>
- [46] J. J. Grainger, W. D. Stevenson, Power System Analysis, McGraw-Hill, 1994, google-Books-ID: 74NB91nQSTEC.